HHS Public Access

Author manuscript

Cell Rep. Author manuscript; available in PMC 2020 September 11.

Published in final edited form as:

Cell Rep. 2020 July 07; 32(1): 107866. doi:10.1016/j.celrep.2020.107866.

Neto-α Controls Synapse Organization and Homeostasis at the *Drosophila* Neuromuscular Junction

Tae Hee Han[1,6], **Rosario Vicidomini**[1,6], **Cathy Isaura Ramos**[1,2,6], **Qi Wang**[1], **Peter Nguyen**[1], **Michal Jarnik**[1], **Chi-Hon Lee**[1,3], **Michal Stawarski**[4,5], **Roberto X. Hernandez**[4], **Gregory T. Macleod**[4], **Mihaela Serpe**[1,7,*]

[1]Cell Biology and Neurobiology Branch, Eunice Kennedy Shriver National Institute of Child Health and Human Development, NIH, Bethesda, MD, USA [2]Institute of Functional Genomics of Lyon, Lyon, France [3]Institute of Cellular and Organismic Biology, Academia Sinica, Taipei, Taiwan [4]Wilkes Honors College and Department of Biology, Florida Atlantic University, Jupiter, FL, USA [5]Biomedical Department, University of Basel, Basel, Switzerland [6]These authors contributed equally [7]Lead Contact

SUMMARY

Glutamate receptor auxiliary proteins control receptor distribution and function, ultimately controlling synapse assembly, maturation, and plasticity. At the *Drosophila* neuromuscular junction (NMJ), a synapse with both pre- and postsynaptic kainate-type glutamate receptors (KARs), we show that the auxiliary protein Neto evolved functionally distinct isoforms to modulate synapse development and homeostasis. Using genetics, cell biology, and electrophysiology, we demonstrate that Neto-α functions on both sides of the NMJ. In muscle, Neto-α limits the size of the postsynaptic receptor field. In motor neurons (MNs), Neto-α controls neurotransmitter release in a KAR-dependent manner. In addition, Neto-α is both required and sufficient for the presynaptic increase in neurotransmitter release in response to reduced postsynaptic sensitivity. This KAR-independent function of Neto-α is involved in activity-induced cytomatrix remodeling. We propose that *Drosophila* ensures NMJ functionality by acquiring two Neto isoforms with differential expression patterns and activities.

In Brief

Han et al. report that Neto-α functions on both pre- and postsynaptic sides of individual synapses at the *Drosophila* NMJ. Postsynaptic Neto-α regulates the organization of glutamate receptor fields, whereas presynaptic Neto-αis required for normal physiology and homeostatic plasticity.

*Correspondence: mihaela.serpe@nih.gov.

AUTHOR CONTRIBUTIONS

Conceptualization, T.H.H., C.I.R., R.V., G.T.M., and M.S.; Methodology, T.H.H., C.I.R., R.V., G.T.M., and M.S.; Investigation, T.H.H., C.I.R., R.V., Q.W., M.J., M.S., and R.X.H.; Writing, T.H.H., C.I.R., R.V., G.T.M., and M.S.; Funding Acquisition, G.T.M. and M.S.; Resources, P.N. and C.-H.L.; Supervision, G.T.M. and M.S.

DECLARATION OF INTERESTS

The authors declare no competing interests.

SUPPLEMENTAL INFORMATION

Supplemental Information can be found online at https://doi.org/10.1016/j.celrep.2020.107866.

Graphical Abstract

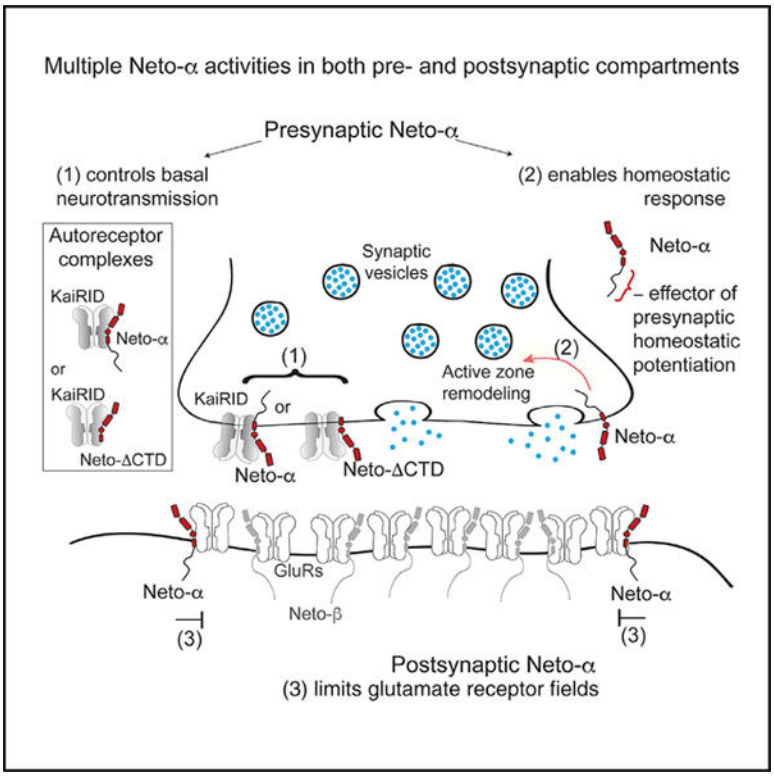

INTRODUCTION

Formation of functional synapses during development and their fine-tuning during plasticity and homeostasis relies on ion channels and their accessory proteins, which control where, when, and how the channels function. Auxiliary proteins are diverse transmembrane proteins that associate with channel complexes and mediate their properties, subcellular distribution, surface expression, synaptic recruitment, and associations with various synaptic scaffolds (Jackson and Nicoll, 2011). Channel subunits have expanded and diversified during evolution to impart different channel biophysical properties (Alberstein et al., 2015; Han et al., 2015; Li et al., 2016; Mayer, 2017), but whether auxiliary proteins have evolved to match channel diversity remains unclear.

Ionotropic glutamate receptors (iGluRs) mediate neurotransmission at most excitatory synapses in the vertebrate CNS and at the neuromuscular junction (NMJ) of insects and crustaceans and include α-amino-3-hydroxy-5-methyl-4-isoxazolepropionic acid receptors (AMPARs), N-methyl-D-aspartic acid receptors (NMDARs), and kainate receptors (KARs). Sequence analysis of the *Drosophila* genome identified 14 iGluRs genes that resemble vertebrate AMPARs, NMDARs, and KARs (Littleton and Ganetzky, 2000). The fly receptors have strikingly different ligand binding profiles (Han et al., 2015; Li et al., 2016); nonetheless, phylogenetic analysis indicates that two of the *Drosophila* genes code for AMPARs, two code for NMDARs, and 10 code for subunits of the KAR family, which is highly expanded in insects (Li et al., 2016). In flies and vertebrates, AMPARs and KARs

have conserved, dedicated auxiliary proteins. For example, AMPARs rely on Stargazin and its relatives to selectively modulate receptors' gating properties, trafficking, and interactions with scaffolds such as PSD-95-like membrane-associated guanylate kinases (Milstein and Nicoll, 2008; Sumioka et al., 2010; Tomita et al., 2003, 2005; Twomey et al., 2016). Stargazin is also required for the functional reconstitution of invertebrate AMPARs (Li et al., 2016; Walker et al., 2006). KARs are modulated by the Neto (Neuropilin and Tolloid-like) family of proteins, including vertebrate Neto1 and Neto2 (Ng et al., 2009; Zhang et al., 2009), *C. elegans* SOL-2/Neto (Wang et al., 2012), and *Drosophila* Neto (Kim et al., 2012; Kim and Serpe, 2013). Neto proteins differentially modulate the gating properties of vertebrate KARs (Tomita and Castillo, 2012). A role for Neto in the biology of KARs *in vivo* has been more difficult to assess because of the low levels of KARs and Neto proteins (Lerma and Marques, 2013). Nevertheless, vertebrate Netos modulate synaptic recruitment of selective KARs by association with synaptic scaffolds such as GRIP and PSD-95, and the PDZ binding domains of vertebrate KAR/Neto complexes are essential for basal synaptic transmission and long-term potentiation (LTP) (Sheng et al., 2018; Tang et al., 2012). Post-translational modifications regulate Neto activities *in vitro*, but the *in vivo* relevance of many of these observations remains unknown (Lomash et al., 2017).

Drosophila NMJ is an excellent genetic system to probe the repertoire of Neto functions. This glutamatergic synapse appears to rely exclusively on KARs, with one presynaptic and five postsynaptic subunits (described later). We previously found that *Drosophila* Neto is an obligatory auxiliary subunit of the postsynaptic KAR complexes (Kim et al., 2012; Kim and Serpe, 2013): in the absence of Neto, postsynaptic KARs fail to cluster at synaptic sites and the animals die as paralyzed embryos. Heterologous reconstitution of postsynaptic KARs in *Xenopus* oocytes revealed that Neto is required for functional receptors (Han et al., 2015). The fly NMJ contains two glutamate receptor (GluR) complexes (types A and B) with different subunit compositions (either GluRIIA or GluRIIB, plus GluRIIC, GluRIID, and GluRIIE) and distinct properties, regulation, and localization patterns (DiAntonio, 2006; DiAntonio et al., 1999; Featherstone et al., 2005; Marrus et al., 2004; Petersen et al., 1997; Qin et al., 2005). The postsynaptic response to the fusion of single synaptic vesicles (quantal size) is reduced for NMJs with type B receptors only, and the dose of GluRIIA and GluRIIB is a key determinant of quantal size (DiAntonio et al., 1999). The fly NMJ is also a powerful model system to study homeostatic plasticity (Davis and Müller, 2015; Frank, 2014). Manipulations that decrease the responsiveness of postsynaptic GluR (leading to a decrease in quantal size) trigger a robust compensatory increase in presynaptic neurotransmitter release or quantal content (QC) (Davis et al., 1998; DiAntonio et al., 1999; Petersen et al., 1997). This increase in QC restores evoked muscle responses to normal levels. A presynaptic KAR, KaiRID, has recently been implicated in basal neurotransmission and presynaptic homeostatic potentiation (PHP) at the larval NMJ (Kiragasi et al., 2017; Li et al., 2016). The role of KaiRID in modulation of basal neurotransmission resembles GluK2/GluK3 function as autoreceptors (Pinheiro et al., 2007). The role of KaiRID in PHP must be indirect, because a mutation that renders this receptor Ca^{2+} impermeable has no effect on the expression of presynaptic homeostasis (Kiragasi et al., 2017).

The fly NMJ reliance on KARs raises the possibility that *Drosophila* diversified and maximized its use of Neto proteins. *Drosophila neto* encodes two isoforms (Neto-α and

Neto-β) with distinct intracellular domains generated by alternative splicing (Ramos et al., 2015). Both cytoplasmic domains are rich in phosphorylation sites and docking motifs, suggesting rich modulation of Neto/KAR distribution and function. Neto-β, the predominant isoform at the larval NMJ, mediates intracellular interactions that recruit PSD components and enables synaptic stabilization of selective receptor subtypes (Ramos et al., 2015). Neto-α can rescue viability and receptor clustering defects of *neto*^{null} (Kim et al., 2012, 2015; Ramos et al., 2015). However, the endogenous functions of Neto-α remain unknown.

Here, we showed that Neto-α is key to synapse development and homeostasis and fulfills functions distinct from those of Neto-β. Using isoform-specific mutants and tissue-specific manipulations, we found that loss of Neto-α in the postsynaptic muscle disrupts GluR fields and produces enlarged PSDs. Loss of presynaptic Neto-α disrupts basal neurotransmission and renders these NMJs unable to express PHP. We mapped the different functions of Neto-α to distinct protein domains and demonstrated that Neto-α is both required and sufficient for PHP, functioning as a bona fide effector for PHP. We propose that *Drosophila* ensured NMJ functionality by acquiring two Neto isoforms with differential expression patterns and activities.

RESULTS

Neto-α and Neto-β Have Distinct Roles during NMJ Development

To study Neto-α function at the *Drosophila* NMJ, we generated isoform-specific *neto-α*^{null} mutants using CRISPR-Cas9 technology (Figure 1A). Several independent lines were isolated and confirmed molecularly as *neto-α* genetic null mutants; all these lines were viable, were fertile, and exhibited no obvious behavior deficits. For further analyses, we selected a line in which 13,476 bp had been deleted, including the α-specific exon and parts of the flanking introns. Elimination of the α-specific exon did not affect the muscle expression of Neto-β, as confirmed by qPCR in larval carcasses (data not shown) and larval muscle western blot (Figure 1B) (Ramos et al., 2015). We tested whether Neto-β is properly targeted at *neto-α*^{null} NMJs using anti-Neto antibodies raised against the extracellular CUB1 domain, common to both Neto isoforms (Kim et al., 2012) (Figures 1C and 1D). Quantification of these NMJ signals relative to anti-horseradish peroxidase (HRP), which labels neuronal membranes (Jan and Jan, 1982), confirmed that Neto-β is the predominant isoform at the fly NMJ (Ramos et al., 2015) and indicated relatively normal synaptic recruitment of Neto-β in the absence of Neto-α.

We previously reported that loss of Neto-β alters the NMJ morphology and produces shorter NMJs with fewer, enlarged type Ib boutons (Ramos et al., 2015). The morphology of *neto-α*^{null} NMJs is strikingly different, with significantly smaller type Ib boutons (Figures 1E–1K). In the absence of Neto-α, the length of individual NMJ segments did not change significantly, but the number of branches increased, producing longer NMJs. Thus, the two Neto isoforms appear to have distinct roles during NMJ growth and development.

Neto-α Is Required for Normal NMJ Physiology

To test whether Neto-α influences NMJ function, we recorded spontaneous miniature excitatory junctional potentials (mEJPs) and evoked excitatory junctional potentials (EJPs) from muscle 6, segment A3, of third-instar larvae of control (w^{1118}) and *neto-α*^{null} animals (Figures 1L–1P; Table S1). No differences were found in the resting potential and input resistance in mutant larvae. The miniature amplitude or quantal size reflects the amount of glutamate released from a single vesicle and the status of postsynaptic receptors. The miniature amplitudes were similar in *neto-α*^{null} and control animals (*neto-α*^{null}, 1.25 ± 0.05 mV, versus w^{1118}, 1.09 ± 0.06 mV; p = 0.07) (Figures 1L and 1N). This differs from *neto-β*^{null} animals, which have significantly reduced postsynaptic type A receptors and decreased quantal size (Ramos et al., 2015). However, *neto-β*^{null} mutants have normal EJP amplitudes, whereas *neto-α*^{null} animals showed EJP amplitudes reduced by 46% (21.62 ± 1.89, compared with 38.60 ± 2.17 in control; p < 0.0001) (Figures 1M and 1O). The QC, estimated as the ratio of the average EJP amplitude to the mEJP amplitude, was decreased in *neto-α*^{null} larvae (19.75 ± 1.63, compared with 31.31 ± 2.40 in control; p = 0.0008) (Figure 1P). In contrast, the *neto-β*^{null} mutants exhibit a robust compensatory increase in QC (Ramos et al., 2015), highlighting the differences between the two Neto isoforms at the *Drosophila* NMJ.

Neto-α^{null} Animals Have Normal Receptor Levels but Enlarged PSDs

Because Neto is key to the synaptic recruitment of postsynaptic KARs, could the defects observed at *neto-α*^{null} NMJs result from altered distribution of synaptic receptors? We first examined the synaptic distribution of GluRIIC, an essential subunit shared by both type A and type B receptors, and of the presynaptic scaffold Bruchpilot (Brp), the fly homolog of the vertebrate active zone protein ELSK/CAST that marks the sites of neurotransmitter release (Kittel et al., 2006; Marrus et al., 2004). The GluRIIC and Brp synaptic signals were in perfect juxtaposition at *neto-α*^{null} NMJs (Figure S1A); the puncta appeared less intense in the absence of Neto-α (described later), but the relative levels of synaptic GluRIIC, as well as net GluRIIC protein in the larval muscle, were normal (Figures S1B–S1D). This is in contrast to *neto-β*^{null} or *neto*^{hypo} mutants, which have normal net levels of receptors in the larval muscle but severely reduced synaptic receptors, presumably by limiting Neto (Kim et al., 2012; Ramos et al., 2015). In addition, in the absence of Neto-α, we could not detect perturbations in the levels of synaptic GluRIIA or GluRIIB, demonstrating that Neto-α does not influence their synaptic recruitment (Figures S1E–S1G). This result is consistent with the normal mEJP amplitude observed at *neto-α*^{null} NMJs.

The mildly reduced GluRIIC signal intensities may indicate alterations in the size and/or organization of receptor fields. We tested this possibility by examining individual PSDs. In *Drosophila*, the PSD-95 ortholog Discs Large (Dlg) does not colocalize with the iGluR fields and instead is adjacent to the PSDs (Guan et al., 1996). Indeed, the boundaries between GluRIIC and Dlg-marked structures were well defined in control boutons but were no longer recognizable at *neto-α*^{null} NMJs (Figures 2A and 2B). Moreover, the 3D reconstructions of these boutons showed no overlap between GluRIIC and Dlg signals in controls but significant overlap in *neto-α*^{null} mutants (Figure S2).

To further characterize this defect, we examined synapses stained for pre- and postsynaptic components using 3D structured illumination microscopy (3D-SIM). The individual synapses were stained with Brp, which accumulates at presynaptic specializations called T-bars (Wagh et al., 2006). The anti-Brp monoclonal antibody NC82 recognizes an epitope on the outer diameter of the T-bars and produces a ring-shaped signal when examined by super-resolution microscopy (Fouquet et al., 2009; Sulkowski et al., 2016). Opposite the T-bars, the PSDs contain iGluR/Neto complexes stabilized by various postsynaptic proteins (Sulkowski et al., 2016). At *neto-α*^{null} synapses, the Brp rings appeared normal (Figures 2C and 2D), but the GluRIIC and Neto signals spread outward, expanding the boundaries of individual PSDs. To quantify these differences in PSD organization, we examined the individual synapses in serial section electron micrographs (Figures 2E–2H). The maximum diameters observed at mutant PSDs were significantly higher than the controls (1,100 nm in *neto-α*^{null} versus 780 nm in *w*^{1118}). In contrast, the *neto-α*^{null} T-bars appeared similar to those of control synapses. These results are consistent with our immunohistochemistry results and indicate that Neto-α limits the size of the postsynaptic receptor fields but has no detectable role in the organization of presynaptic specializations.

Neto-α Functions in Both Pre- and Postsynaptic Compartments

We next asked whether Neto-α activities are restricted to the postsynaptic compartment using tissue-specific rescue and knockdown experiments. We found that expression of *neto-α* in motor neurons (MNs) did not rescue the PSD sizes of *neto-α*^{null} synapses, which remained enlarged (Figures 3A–3C and 3E). However, muscle overexpression of a *neto-α* transgene fully rescued the PSD size of *neto-α*^{null} synapses to a mean indistinguishable from control (Figures 3A, 3D, and 3E). Even though the PSD sizes were variable, their relative frequency distribution showed that *neto-α*^{null} PSDs were consistently larger than the control (Figure 3F). This was also captured by the right shifted cumulative frequency distribution of the observed *neto-α*^{null} PSDs (Figure 3G). Again, the distribution of neuron rescue PSDs was similar to that of *neto-α*^{null} mutants, whereas the muscle rescue PSDs resembled the distribution of control PSDs. This indicates that Neto-α functions in the muscle to limit postsynaptic receptor fields. This conclusion was supported by knockdown experiments (data not shown).

Surprisingly, muscle overexpression of *neto-α* did not rescue the neurotransmission defects of *neto-α*^{null} mutants (Figures 3H–3J; Table S1). The EJP amplitude and QC remained severely reduced in these animals (*G14-Gal4* rescue EJP, 16.84 ± 1.49 mV, and QC, 17.71 ± 1.19). However, neuronal expression of *neto-α* restored all these parameters to control levels (*OK6-Gal4* rescue EJP, 36.59 ± 2.78 mV, and QC, 32.30 ± 2.47). We confirmed these results with multiple MN-specific promoters (*OK6-Gal4* shown in Figures 3H–3J and *BG380-Gal4* shown later). Furthermore, knockdown of Neto-α in neurons, but not in muscles, recapitulated the electrophysiological phenotypes of *neto-α*^{null} mutants (*BG380>neto-α*^{RNAi} EJP, 15.45 ± 1.51 mV, and QC, 14.15 ± 1.13; *G14>neto-α*^{RNAi} EJP, 31.73 ± 2.22 mV, and QC, 24.83 ± 3.40).

Altogether, these data suggest that Neto-α functions in both MNs and muscles. In muscles, Neto-α limits PSD size, whereas in MNs, Neto-α has critical roles in ensuring normal

neurotransmitter release. These functions and the low endogenous level of Neto-α are in sharp contrast to those of Neto-β, the predominant isoform at larval NMJ. Unlike Neto-α, Neto-β is required for the synaptic recruitment and stabilization of GluRs (Ramos et al., 2015). The *neto-β*^{null} NMJs have greatly diminished postsynaptic receptors and thus reduced miniature amplitudes (quantal size) but have normal basal neurotransmission because of a compensatory increase in QC. In contrast, both basal neurotransmission and QC are diminished in the absence of Neto-α, suggesting homeostasis deficits.

Loss of Homeostatic Plasticity at *Neto-α*^{null} NMJs

We tested for a role for Neto-α in the homeostatic control of synaptic function using well-studied chronic and acute homeostasis paradigms (Frank et al., 2006). Deletion of the *GluRIIA* subunit greatly diminishes the quantal size throughout NMJ development; this triggers increased QC that restores the evoked muscle responses to normal levels (DiAntonio et al., 1999). In our hands, the *GluRIIA*^{null} mutants had mEJPs reduced by 50%, QC increased by 58%, and relatively normal EJP amplitude (Figures 4A and 4B; Table S1). This presynaptic compensatory response did not occur in the absence of Neto-α; the EJP amplitude was reduced in *neto-α*^{null}; *GluRIIA*^{null} double mutants at levels lower than any individual mutant. These double mutants have reduced mEJPs and lack homeostatic increase in QC. These results are reminiscent of a previously described hypomorphic allele of *neto* (*neto*^{hypo}) with severe deficits in homeostatic plasticity (Kim et al., 2012).

To examine the speed of the Neto-α-mediated homeostatic response, we used an acute homeostasis paradigm that uses philanthotoxin-343 (PhTx), an effective GluR blocker (Frank et al., 2006). PhTx applications to dissected NMJ preparations trigger significant homeostatic compensation within 10 min. Indeed, in control NMJ preparations exposed to 20 μM PhTx, we observed a strong decrease of mEJP amplitude (from 1.25 ± 0.05 to 0.69 ± 0.04 mV) and a robust compensatory response, with QC increasing from 31.31 ± 2.40 to 47.13 ± 2.77 (Figures 4C, 4D, and S3A). PhTx applications also triggered reduced mEJP at *neto-α*^{null} NMJs (from 1.09 ± 0.06 to 0.74 ± 0.03 mV); however, *neto-α*^{null} did not show changes in QC. Similar recordings performed at a higher Ca^{2+} concentration (0.8 mM Ca^{2+}) showed higher EJP amplitudes at both control and *neto-α*^{null} NMJs (Table S1). Nevertheless, no substantial compensatory response/increase in QC was observed in the absence of Neto-α (66.95 ± 5.48 before and 73.15 ± 6.26 after PhTx), whereas the control showed an 80% increase in QC (from 50.80 ± 3.20 before to 91.53 ± 5.19 after PhTx). These results demonstrate that Neto-α is critical for both chronic and acute homeostatic modulation of neurotransmitter release in response to reduced postsynaptic sensitivity.

We next tested the tissue-specific requirements for Neto-α in homeostatic plasticity using rescue experiments and acute PhTx applications. Overexpression of *neto-α* in MNs, but not in muscles, significantly rescued the PhTx-induced increase in QC at *neto-α*^{null} NMJs (to 48.97 ± 5.60 in *Neto-α*^{null}; *OK6>neto-α* versus 17.31 ± 2.35 in *neto-α*^{null}; *G14>neto-α*) (Figures 4E, 4F, and S3B). Altogether, these results demonstrate that Neto-α functions in MNs to modulate basal neurotransmission and to confer homeostatic plasticity. Because rapid homeostatic compensation occurs in NMJ preparations with severed motor axons, in the absence of either protein translation or action potential (AP) evoked neurotransmission

(Frank et al., 2006), these results suggest that Neto-α functions in the presynaptic terminals or is developmentally required for a presynaptic activity necessary for PHP.

Using an antisense probe specific to the Neto-α intracellular domain, we found that *neto-α* transcript is expressed in the striated muscle starting from late embryo stages through larval stages (third-instar control and *neto-α*^{null} shown in Figures 5A and 5B). *neto-α* expression was also detected in a subset of cells in the larval CNS. Overexpression of GFP-tagged Neto-α in MNs produced accumulation of Neto-α-positive signals in the somato-dendritic compartments, along the axons, and at synaptic terminals, close to the Brp-marked active zones (Figures 5C and 5C'). To examine Neto-β-specific signals, we took advantage of a previously described *neto-β*^{short} allele that produces a Neto-β variant with a short cytoplasmic tail (122 residues instead of 351) (Ramos et al., 2015). This truncated Neto-β short lacks the last 229 amino acids, including the b1 epitope, allowing specific detection of neuronally expressed full-length *neto-β*. Intriguingly, neuronal overexpression of Neto-β did not induce accumulation along axons or at synaptic terminals; instead, Neto-β remained restricted to the somato-dendritic compartment (Figure 5D).

The GFP tag does not interfere with the presynaptic functions of Neto-α: tagged Neto-α rescued basal neurotransmission of *neto-α*^{null} mutants as effectively as unmodified Neto-α (Figures 5E and 5F). In addition, expression of Neto-α-GFP in the MNs was similar to Neto-α in restoring the acute homeostatic response at *neto-α*^{null} NMJs (Figures 5H, 5I, and S3C). More specifically, neuronal expression of *neto-α* or *neto-α-GFP* rescued the EJP amplitude in *neto-α*^{null} mutants to 36.33 ± 1.90 and 38.69 ± 1.97 mV, respectively; in response to PhTx application, QC increased from 32.74 ± 2.12 to 63.30 ± 2.93 in *neto-α*-rescued mutants and from 31.54 ± 2.66 to 49.08 ± 1.82 in *neto-α-GFP*-rescued animals. In contrast, expression of *neto-β* in MNs could not rescue basal neurotransmission or homeostatic potentiation at *neto-α*^{null} NMJs (Figures 5G and 5H). These larvae exhibit reduced basal neurotransmission (19.73 ± 1.89 mV before and 9.39 ± 1.25 mV after PhTx application) and no compensatory increase in QC (16.00 ± 1.20 versus 14.97 ± 2.02), resembling the *neto-α*^{null} NMJs. Lack of Neto-β-mediated neuronal rescue could reflect the inability of Neto-β to localize to presynaptic terminals and/or to fulfill the Neto-α-specific functions in MNs. These results uncover isoform-specific functions for Neto-α at the *Drosophila* NMJ and suggest that Neto-α functions in the presynaptic terminal.

Neto-α Enables Fast Recruitment of the Active Zone Protein Brp

The neurotransmission defects at *neto-α*^{null} NMJs may reflect deficits in presynaptic Ca^{2+} entry. We investigated this possibility using a Ca^{2+}-sensitive fluorescent dye loaded into motor nerve terminals (Macleod, 2012). This dye fluoresces in proportion to free Ca^{2+} levels in the cytosol ($[Ca^{2+}]_c$). When loaded in constant proportion to a Ca^{2+}-insensitive dye, it allows ratiometric comparisons between *neto-α*^{null} and control type Ib and type Is terminals (Figure 6A). $[Ca^{2+}]_c$ at rest, estimated before stimulation, was no different in *neto-α*^{null} relative to control (Figure 6B) (Ib, $p = 0.85$; Is, $p = 0.96$). The amplitude and decay of single-AP evoked changes in $[Ca^{2+}]_c$ in response to 1 Hz nerve stimulation were no different in *neto-α*^{null} (Figures 6C and 6D) (amplitude: Ib, $p = 0.62$; Is, $p = 0.96$) (decay: data not shown; Ib, $p = 0.42$; Is, $p = 0.56$). Finally, the Ca^{2+} signals evoked by 10 and 20 Hz stimulus

trains were no different in *neto-α*^{null} (10 Hz, data not shown; Ib, p = 0.63; Is, p = 0.93) (20 Hz; Ib, p = 0.37; Is, p = 0.40) (Figure 6E). Although the data shown here are sufficiently sensitive to reveal the differences in Ca^{2+} entry known to exist between type Ib and type Is terminals (He et al., 2009; Lu et al., 2016), they reveal no deficit in Ca^{2+} entry in *neto-α*^{null} terminals. Thus, *neto-α*^{null} neurotransmission deficits are most likely the result of deficits in the release apparatus downstream of Ca^{2+} entry.

To estimate the number of release-ready presynaptic vesicles in *neto-α*^{null} mutants, we analyzed cumulative postsynaptic current during high-frequency stimulus trains (30 stimuli at 50 Hz) (Müller et al., 2012) (Figures 6F–6H). We measured evoked excitatory junction currents (EJCs) at a voltage clamped to —65 mV, in HL-3 (hemolymph-like solution 3) (Stewart et al., 1994) saline with 1.5 mM Ca^{2+} and 10 mM Mg^{2+} and cumulative EJCs evoked by 50 Hz stimulation (30 stimuli) of control and *neto-α*^{null} NMJs. Back-extrapolation from linear fits to the cumulative EJC to time zero yielded 418 ± 22 vesicles for control and 451 ± 18 vesicles for *neto-α*^{null} (n = 5, p = 0.28). Finally, the size of the readily released pool (RRP) was calculated; there was no significant difference between control (522 ± 28, n = 5) and *neto-α*^{null} (581 ± 24, n = 5, p = 0.14). This indicates that the absence of Neto-α does not alter the basal RRP size and therefore could not cause the observed reduced basal neurotransmission.

Previous studies showed that PhTx application results in a rapid increase in the quantity of presynaptic active zone protein Brp, accompanied by an elaboration of the presynaptic cytomatrix structure (Goel et al., 2017; Weyhersmüller et al., 2011). We quantified the Brp puncta before and after PhTx exposure and confirmed that upon PhTx application, control NMJs showed a significant increase (27.50% ± 0.07%) in Brp-positive immunoreactivities (Figures 6I and 6K). However, no increase in the Brp-positive signals was detectable at *neto-α*^{null} NMJs (Figures 6J and 6K). Furthermore, relative frequency and cumulative probability distributions of Brp intensities revealed a rightward shift in PhTx-treated control NMJs, but not *neto-α*^{null} NMJs (Figures 6L and 6M). These findings suggest that in response to PhTx-triggered reduced postsynaptic sensitivity, Neto-α functions to swiftly mobilize Brp, which presumably enhances vesicle release and enables the compensatory response.

Distinct Domains of Neto-α Regulate Basal Release and Presynaptic Potentiation

We previously demonstrated that a minimal Neto variant called Neto-ΔCTD, which contains the highly conserved domains shared by Neto-α and Neto-β (the extracellular CUB domains, LDLa motif, and the transmembrane part) but has no intracellular C-terminal domain, is both required and sufficient for the synaptic recruitment and function of postsynaptic KARs (Ramos et al., 2015). To examine the expression level and the subcellular distribution of the *neto-ΔCTD* transgene, we used the apical localization of Neto in epithelial tissues. *BG380-Gal4* drives the expression of *UAS* transgenes in MNs and in salivary glands. We found that Neto-α-GFP and Neto-ΔCTD-GFP expressed at comparable levels at both synaptic terminals and in the salivary glands and localized to the luminal/apical side of the salivary glands (Figure S4). Neuronal overexpression of Neto-ΔCTD-GFP recapitulated the Neto-α-GFP distribution and localized to dendrites and soma, along axons, and at synaptic terminals (Figures 7A, 7B, and 5C). Neuronal Neto-ΔCTD-GFP rescued

basal neurotransmission at *neto-α*^{null} mutant NMJs (EJP, 37.15 ± 0.98 mV, and QC, 38.97 ± 1.67) (Figures 7C and 7C′). This indicates that Neto-ΔCTD is sufficient for normal baseline. However, this variant could not rescue the acute PHP response in *neto-α*^{null} mutants (Figure 7C″). Instead, upon PhTx exposure, the QC decreased from 38.97 ± 1.67 to 23.47 ± 2.78 at these NMJs, indicating that the intracellular part of Neto-α, although dispensable for basal neurotransmission, is required for PHP.

Because Neto proteins modulate the function of KARs, the phenotypic similarities between *neto-α*^{null} and *KaiRID* loss-of-function mutants indicate that Neto-α may partly function by modulating the presynaptic KaiRID. In both mutants, neuronal expression of the corresponding full-length transgenes rescued basal neurotransmission and PHP deficits: KaiRID loss of function in Kiragasi et al. (2017) and *neto-α*^{null} (Figure 4). However, a Ca^{2+}-impermeable variant (*KaiRID*^{R}) restored the presynaptic homeostasis at *KaiRID* mutant NMJs but did not rescue basal neurotransmission (Kiragasi et al., 2017; Li et al., 2016). Because presynaptic Neto-ΔCTD efficiently rescued the EJP amplitudes at *neto-α*^{null} NMJs but only full-length Neto-α rescued their PHP, Neto-α may (1) engage KaiRID and modulate basal neurotransmission via KaiRID/Neto-ΔCTD complexes and (2) confer homeostatic potentiation via its intracellular domain.

We tested this model by first generating a *KaiRID*^{null} mutant using the CRISPR-Cas9 methodology and comparing the phenotypes of single and double (*neto-α*^{null} and *KaiRID*^{null}) mutants (Figures 7D and 7E). The *KaiRID*^{null} neurotransmission defects were fully rescued by expression of KaiRID in MNs, confirming the specificity of the molecular lesion (Table S1). Basal neurotransmission defects observed at *KaiRID*^{null} synapses resembled the phenotypes reported for *KaiRID* loss-of-function alleles (Kiragasi et al., 2017) and were not significantly different from the defects observed for *neto-α*^{null} mutants (Figures 7D and S5). The *KaiRID*^{null} defects were evident at higher Ca^{2+} concentration than the previously published *KaiRID* alleles, suggesting that the genetic null described here has a more penetrant phenotype. More importantly, the *neto-α*^{null}*;;KaiRID*^{null} double mutant showed basal neurotransmission phenotypes similar to the individual single mutants (Figures 7E and S5). These results suggest that Neto-α and KaiRID function together in MNs to control basal neurotransmission. *neto-α*^{null} and *KaiRID*^{null} single and double mutants were similarly impaired in their acute PHP responses (Figures 7D and 7E; Table S1).

Because the intracellular part of Neto-α is key to PHP, we examined whether expression of Neto-α-GFP in MNs could partly rescue the neurotransmission defects at *neto-α*^{null}*;;KaiRID*^{null} NMJs. As expected, neuronal expression of Neto-α-GFP or Neto-ΔCTD-GFP did not rescue basal neurotransmission at *neto-α*^{null}*;;KaiRID*^{null} NMJs, which remained at 17.45 ± 1.56 and 17.36 ± 3.12 mV, respectively (Figures 7F and S6; Table S1). This is consistent with a KaiRID-dependent role for Neto-α in the control of basal neurotransmission. However, neuronal expression of Neto-α-GFP significantly restored the homeostatic response in *neto-α*^{null}*;;KaiRID*^{null} mutants; their QC was 15.03 ± 156 before and 24.63 ± 2.67 after PhTx, an increase of 64%. Furthermore, neuronal overexpression of Neto-α in the *KaiRID*^{null} single-mutant background exacerbated the amplitude of the PHP response as the QC increased from 11.95 ± 1.83 before to 29.31 ± 2.81 after PhTx (Figure 7G). No such change was observed in control *KaiRID*^{null} animals with *UAS-neto-α*

transgene but no driver, in which the QC was 18.95 ± 0.75 before and 17.81 ± 1.21 after PhTx (Table S1). This indicates that (1) Neto-α is sufficient for presynaptic homeostasis and (2) endogenous levels of Neto-α are limiting. Altogether, these data demonstrate that the two major functions of Neto-α in the presynaptic compartment could be segregated and mapped to different domains: (1) the minimal Neto, or Neto-ΔCTD, which modulates basal neurotransmission, likely by modulating the KaiRID function, and (2) the intracellular part of Neto-α, which is both required and sufficient for the presynaptic homeostatic response.

DISCUSSION

The fly NMJ is a glutamatergic synapse that uses at least six distinct KAR subunits; they form two distinct postsynaptic complexes (type A and type B) that co-exist within individual PSDs and enable NMJ functionality and plasticity and a presynaptic KaiRID-containing complex that modulates basal neurotransmission. Here we show that Neto-α is required in both pre- and postsynaptic compartments for the proper organization and function of the *Drosophila* NMJ. In muscle, Neto-α limits the size of the postsynaptic receptor field; the PSDs are significantly enlarged in muscle where Neto-α has been perturbed (Figures 2 and 3). In MNs, Neto-α is required for two distinct activities: (1) modulation of basal neurotransmission in a KaiRID-dependent manner and (2) effector of presynaptic homeostasis response. To our knowledge, this is an extremely rare example of a GluR auxiliary protein that modulates receptors on both sides of a particular synapse and plays a distinct role in homeostatic plasticity.

Vertebrate KARs depend on Neto proteins for their distribution and function (Copits and Swanson, 2012). Because of their reliance on KARs, *Drosophila neto*^{null} mutants have no functional NMJs (no postsynaptic KARs) and consequently die as paralyzed embryos (Kim et al., 2012). We previously showed that muscle expression of Neto-ΔCTD, or minimal Neto, at least partly rescues the recruitment and function of KARs at synaptic locations (Han et al., 2015; Kim et al., 2012, 2015; Ramos et al., 2015). Here we report that neuronal Neto-ΔCTD also rescues the KaiRID-dependent basal neurotransmission (Figure 7). Thus, Neto-ΔCTD, the part of Neto conserved from worms to humans, seems to represent the Neto core required for KAR modulatory activities.

The intracellular parts of Neto proteins are highly divergent, likely reflecting the microenvironments in which different Neto proteins operate (Copits and Swanson, 2012; Tomita, 2010). Similar to mammalian Neto1 and Neto2, *Drosophila* Neto-α and Neto-β are differentially expressed in the CNS (data not shown) and have different intracellular domains that mediate distinct functions. These large intracellular domains are rich in putative phosphorylation sites and docking motifs and could further modulate the distribution and function of KARs or serve as signaling hubs and protein scaffolds. Post-translational modifications regulate vertebrate Neto activities *in vitro*, although the *in vivo* relevance of these changes remains unknown (Lomash et al., 2017). Our data demonstrate that Neto-α and Neto-β could not substitute for each other (this study; Ramos et al., 2015). For example, Neto-β, but not Neto-α, controls the recruitment of PAK, a PSD component that stabilizes selective KAR subtypes at the NMJ, and ensures proper postsynaptic differentiation (Ramos et al., 2015). Conversely, postsynaptic Neto-β alone cannot maintain

a compact PSD size; muscle Neto-α is required for this function (Figure 3). Neto-β cannot fulfill presynaptic functions of Neto-α, presumably because is confined to the somato-dendritic compartment and cannot reach the synaptic terminals (Figure 5D). Histology and western blot analyses indicate that Neto-α constitutes less than 1/10th of the net Neto at the *Drosophila* NMJ (Figure 1) (Ramos et al., 2015). These low levels impaired our ability to directly visualize endogenous Neto-α. We have generated several isoform-specific antibodies, but they could only detect Neto-α when overexpressed (data not shown). Similar challenges have been encountered in the vertebrate Neto field (Wyeth et al., 2017).

The two Neto isoforms are limiting in different synaptic compartments. Neto-β limits the recruitment and synaptic stabilization of postsynaptic KARs (Ramos et al., 2015). In contrast, several lines of evidence indicate that Neto-α is limiting in MNs. First, overexpression of KaiRID cannot increase basal neurotransmission (Kiragasi et al., 2017); however, neuronal overexpression of Neto-ΔCTD increases basal neurotransmission (Table S1), indicating that Neto, but not KaiRID, is limiting in the MNs. Second, neuronal overexpression of Neto-α exacerbates the PHP response to PhTx exposure and even rescues this response in $KaiRID^{null}$ (Figure 7). These findings suggest that KaiRID's function during PHP is to help traffic and stabilize Neto-α, a low-abundance PHP effector. Similarly, studies in mammals reported that KARs trafficking in the CNS do not require Neto proteins; instead, KARs regulate the surface expression and stabilization of Neto1 and Neto2 (Straub et al., 2011; Zhang et al., 2009). Nonetheless, the KAR-mediated stabilization of Neto proteins at CNS synapses supports KAR distribution and function. In flies, KaiRID-dependent Neto-α stabilization at synaptic terminals ensures KAR-dependent function, normal basal neurotransmission, and Neto-α-specific activity as an effector of PHP.

Previous studies showed that presynaptic KARs regulate neurotransmitter release; however, the site and mechanism of action of presynaptic KARs have been difficult to pin down (Perrais et al., 2010). This study provides strong evidence for Neto activities at presynaptic terminals. First, Neto-α is both required and sufficient for PHP (Figures 4 and 7). It has been shown that the PhTx-induced expression of PHP occurs even when the MN axon is severed (Frank et al., 2006). In addition, the signaling necessary for PHP expression is restricted to postsynaptic densities and presynaptic boutons (Li et al., 2018). Second, Neto-ΔCTD, but not Neto-β, rescued basal neurotransmission defects in $neto\text{-}\alpha^{null}$ (Figures 5 and 7). Both variants contain the minimal Neto required for KAR modulation (Ramos et al., 2015), but only Neto-ΔCTD can reach the presynaptic terminal, whereas Neto-β is restricted to the somato-dendritic compartment. This suggests that Neto-ΔCTD (or Neto-α), together with KaiRID, localizes at presynaptic terminals, where KaiRID could function as an autoreceptor. Finally, upon PhTx exposure, Neto-α enabled fast recruitment of Brp at the active zone (Figure 6). Multiple homeostasis paradigms trigger Brp mobilization, followed by remodeling of presynaptic cytomatrix (Goel et al., 2017). These localized activities support Neto-α functioning at presynaptic terminals.

Presynaptic activities for Neto-α include KaiRID modulation (Li et al., 2016; this study). Rapid application of glutamate to outside-out patches from HEK cells transfected with KaiRID indicated that KaiRID forms rapidly desensitizing channels (Li et al., 2016); addition of Neto increases the desensitization rates and open probability for this channel

(T.H.H., unpublished data). Neto-α has a large intracellular domain (250 residues) rich in post-translational modification sites and docking motifs, including putative phosphorylation sites for Ca^{2+}/calmodulin-dependent protein kinase II (CaMKII), protein kinase C (PKC), and protein kinase A (PKA). This intracellular domain may engage in finely tuned interactions that allow Neto-α to (1) further modulate the KaiRID properties and distribution in response to cellular signals and (2) function as an effector of presynaptic homeostasis in response to low postsynaptic GluR activity. Mammalian Neto1 and Neto2 are phosphorylated by multiple kinases *in vitro* (Lomash et al., 2017); CaMKII- and PKA-dependent phosphorylation of Neto2 restrict GluK1 targeting to synapses *in vivo* and *in vitro*. Similarly, Neto-α may function in a kinase-dependent manner to stabilize KaiRID and/or other presynaptic components. Second, Neto-α may recruit Brp (Figure 6) or other presynaptic molecules that mediate activity-related changes in glutamate release at the fly NMJ. Besides Brp, several presynaptic components have been implicated in the control of PHP (Frank, 2014). They include (1) Cacophony (Cac), the α1 subunit of Ca_V2-type calcium channels and its auxiliary protein α2δ−3, that control the presynaptic Ca^{2+} influx (Müller and Davis, 2012; Wang et al., 2016); (2) the signaling molecules Eph, Ephexin, and Cdc42 upstream of Cac (Frank et al., 2009); and (3) the BMP pathway components, Wit and Mad, required for retrograde BMP signaling (Goold and Davis, 2007). In addition, expression of PHP requires molecules that regulate vesicle release and the RRP size, such as RIM (Müller et at., 2012), Rab3-GAP (Müller et al., 2011), Dysbindin (Dickman and Davis, 2009), and SNAP25 and Snapin (Dickman et al., 2012). Recent studies demonstrated that *trans*-synaptic Semaphorin/Plexin interactions control synaptic scaling in cortical neurons in vertebrates (Wang et al., 2017) and drive PHP at the fly NMJ (Orr et al., 2017). Neto-α may interact with one or several such presynaptic molecules and function as an effector of PHP. Future studies on what the Neto-α cytoplasmic domain binds to and how is it modulated by post-translational modifications should provide key insights into the understanding of molecular mechanisms of homeostatic plasticity.

On the muscle side, Neto-α activities may include (1) engaging scaffolds that limit the PSD size and (2) modulating postsynaptic KAR distribution and function. For example, Neto-α may recruit *trans*-synaptic complexes such as Ten-a/Ten-m or Nrx/Nlgs that have been implicated in limiting the postsynaptic fields (Banovic et al., 2010; Mosca et al., 2012). In particular, DNlg3, like Neto-α, is present in both pre- and postsynaptic compartments and has similar loss-of function phenotypes, including smaller boutons with larger individual PSDs, and reduced EJP amplitudes (Xing et al., 2014). Neto-α may also indirectly interact with the *Drosophila* PSD-95 and Dlg and help establish the PSD boundaries (Figure 2). Fly Netos do not have PDZ binding domains, but the postsynaptic Neto/KAR complexes contain GluRIIC, a subunit with a class II PDZ binding domain (Marrus et al., 2004). It has been reported that mutations that change the NMJ receptors' gating behavior alter their synaptic trafficking and distribution (Petzoldt et al., 2014). Neto-α could be key to these observations, because it may influence both receptor gating properties and ability to interact with synapse organizers.

Phylogenetic analyses indicate that Neto-β is the ancestral Neto. In insects, Neto-β is predicted to control NMJ development and function, including recruitment of iGluRs and PSD components, and postsynaptic differentiation (Ramos et al., 2015). Neto-α appears to

be a rapidly evolving isoform present in higher *Diptera*. This large order of insects is characterized by a rapid expansion of the KAR branch to ten distinct subunits (Li et al., 2016). Insect KARs have unique ligand binding profiles, strikingly different from vertebrate KARs. However, like vertebrate KARs, they all seem to be modulated by Neto proteins. We speculate that the rapid expansion of KARs forced the diversification of the relevant accessory protein, Neto, and the extension of its repertoire. In flies, the *neto* locus acquired an additional exon and consequently an alternative isoform with distinct expression profiles, subcellular distributions, and isoform-specific functions. It will be interesting to investigate how flies differentially regulate the expression and distribution of the two Neto isoforms and control their tissue- and synapse-specific functions. Mammals have five KAR subunits, three of which have multiple splice variants that confer rich regulation (Lerma and Marques, 2013). In addition, mammalian Neto proteins have fairly divergent intracellular parts that presumably further integrate cell-specific signals and fine-tune KAR localization and function. In *Diptera*, KARs have relatively short C tails and thus limited signaling input, whereas Netos have long cytoplasmic domains that could function as scaffolds and signaling hubs. Consequently, most information critical for NMJ assembly and postsynaptic differentiation has been outsourced to the intracellular part of Neto-β (Ramos et al., 2015). Neto-α-mediated intracellular interactions may also hold key insights into the mechanisms of homeostatic plasticity. Our study reveals that Neto functions as a bona fide effector of presynaptic homeostasis.

STAR METHODS

Detailed methods are provided in the online version of this paper and include the following:

RESOURCE AVAILABILITY

Lead Contact—Further information and requests for resources and reagents should be directed to and will be fulfilled by the Lead Contact, Mihaela Serpe (mihaela.serpe@nih.gov).

Materials Availability—*Drosophila* lines generated in this study are available upon request.

Data and Code Availability—This study did not generate datasets/code.

EXPERIMENTAL MODEL AND SUBJECT DETAILS

The *neto-α*^{null} and *KaiRID*^{null} alleles were generated using classic CRISPR/Cas9 methodology as previously described (Gratz et al., 2015). Briefly, for each allele, two pairs of gRNAs were injected in *y sc v; [nos-Cas9]attP40/CyO* stock (Ren et al., 2013) followed by germline transformation (Rainbow transgenics). A series of unmarked deletions were isolated and molecularly characterized by PCR from genomic DNA (QuickExtractDNA, Epicenter) and sequencing. Putative genetic null alleles have been isolated and confirmed by sequence analysis; they were subsequently moved in an w^{1118} background and balanced with markers visible during larval stages. The primers used for gRNAs, PCR and sequencing were as follows:

alpha-1 sense: CTTCGGTTTCTGGGGATAAGATGG

alpha-1 antisense: AAACCCATCTTATCCCCAGAAACC

alpha-3 sense: CTTCGGAATATAATGGAAAAATGA

alpha-3 antisense: AAACTCATTTTTCCATTATATTCC

Neto-F1: AGTCCCTTTACCACTCCATTAGCC

Neto-R1: TTGCGAGTGCTTTTGCCTGC

CG3822-gATD1 sense: CTTCGCATTTTGAATTCGTTCGCGA

CG3822-gATD1 antisense: AAACTCGCGAACGAATTCAAAATGC

CG3822-gATD2 sense: CTTCGACAGCTTCCATGCCGGGAAA

CG3822-gATD2 antisense: AAACTTTCCCGGCATGGAAGCTGTC

CG3822-F1: CAAACCCTTGGAGAAATAGGG

CG3822-R1: CTACGATTGAGGTCCCCTTG.

Neto-F1/R1 are predicted to amplify a 15kb product from control animals and 2kb from *neto-α*^{null}. Line #117 missing 13kb (13,506,327–13,519,803), including the entire alpha-specific exon, was selected as *neto-α*^{null}.

CG3822-F1/R1 are predicted to amplify a 994bp product from control animals, and 444bp from *KaiRID*^{null}. Line #19 has a truncated message that codes for the first 79 residues of KaiRID, followed by three different amino acids and a stop codon.

Other fly stocks used in this study were as follows: *neto*^{null} and *neto*^{hypo} (Kim et al., 2012); *UAS-neto-α* (line A9), *UAS-neto-α-GFP* (line B4) (Kim et al., 2015); *neto-β*^{null}, *neto-β*^{short}, *UAS-neto-β* (line NB6), *UAS-neto*D*CTD-GFP* (line H6y), *neto-α*^{RNAi}, *neto-β*^{RNAi} (Ramos et al., 2015), *GluRIIA*^{SP16} and *Df(2L)cl*^{h4} (Petersen et al., 1997) (from A. DiAntonio, Washington University). The *G14-Gal4*, *BG380-Gal4*, and *OK6-Gal4* were previously described.

Flies were reared on Jazz-Mix food (Fisher Scientific) at 25°C and analyzed at the third instar larval stage.

METHOD DETAILS

Protein analysis and immunohistochemistry—To analyze muscle proteins, wandering third instar larvae were dissected, and all tissues except for the body wall (muscle and cuticle) were removed. The body walls were mechanically disrupted and lysed in lysis buffer (50 mM Tris-HCl, 150 mM NaCl, 1% Triton X-100, 1% deoxycholate, protease inhibitor cocktail (Roche) for 30 min on ice. The lysates were separated by SDS-PAGE on 4%–12% NuPAGE gels (Invitrogen) and transferred onto PVDF membranes (Millipore).

Primary antibodies were used at the following dilutions: rat anti-Neto-ex (Kim et al., 2012), 1:1000; anti-Tubulin (Sigma-Aldrich),1:1000.

For immunohistochemistry, wandering third instar larvae of the desired genotypes were dissected in ice-cooled Ca^{2+}-free HL-3 solution (70 mM NaCl, 5 mM KCl, 20 mM $MgCl_2$, 10 mM $NaHCO_3$, 5 mM trehalose, 5 mM HEPES, 115 mM sucrose) (Stewart et al., 1994; Budnik et al., 1996). The samples were fixed in 4% paraformaldehyde (PFA) (Polysciences, Inc.) for 20 min or in Bouin's fixative (Bio-Rad) for 3 min and washed in PBS containing 0.5% Triton X-100. For PhTx treatment, third instar larvae were pinned anteriorly and posteriorly, dissected along the dorsal midline and incubated either with 10 mM PhTx for 15 min in Ca^{2+}-free HL-3, or without PhTx for the control. PhTx was then washed out, the fat body and guts were removed, and the fillets were fixed in 4% PFA for 20 min, then processed normally.

Primary antibodies from Developmental Studies Hybridoma Bank were used at the following dilutions: mouse anti-GluRIIA (MH2B), 1:100; mouse anti-Dlg (4F3), 1:1000; mouse anti-Brp (Nc82), 1:200. Other primary antibodies were utilized as follow: rat anti-Neto-ex, 1:1000 (Kim et al., 2012); rabbit anti-Neto-β (raised against the synthetic peptide b1), 1:1,000, rabbit anti-GluRIIC, 1:2,000, rabbit anti-GluRIIB, 1:1,000, (Ramos et al., 2015); chicken anti-GFP, 1:1,000, (Abcam); and Cy5- conjugated goat anti-HRP, 1:1000 (Jackson ImmunoResearch Laboratories, Inc.). Alexa Fluor 488-, Alexa Fluor 568-, and Alexa Fluor 647-conjugated secondary antibodies (Molecular Probes) were used at 1:200. Samples were mounted in antifade reagents ProLong Gold or SlowFade Gold with DAPI (Invitrogen).

Samples of different genotypes were processed simultaneously and imaged under identical confocal settings in the same imaging session with a laser scanning confocal microscope (CarlZeiss LSM780, 40X ApoChromat, 1.4 NA, oil immersion objective). All images were collected as 0.2 μm (for NMJ) or 0.1 μm (for individual synapses) optical sections and the *z*-stacks were analyzed with Imaris software (Bitplane) or ImageJ (NIH) respectively.

NMJ morphometrics were performed as previously described (Ramos et al., 2015). Briefly, positive puncta were detected semiautomatically using the spot finding Imaris algorithm. To quantify fluorescence intensities, synaptic ROI areas surrounding anti-HRP immunoreactivities were selected and the signals measured individually at NMJs (muscle 6/7 or muscle 4, segment A3) from 10 or more different larvae for each genotype. The signal intensities were calculated relative to HRP volume and subsequently normalized to control. Morphometric quantifications such as branching points and branch length were quantified semi-automatically with Filament algorithm. Boutons were counted in preparations double labeled with anti-HRP and anti-Dlg; boutons volume were estimated by manual selection and Spot algorithm (Imaris). All quantifications were performed while blinded to genotype. Statistical analyses were performed using the Student t test with a two-tailed distribution and a two-sample unequal variance. Error bars in all graphs indicate standard deviation ± SEM. ****, $p < 0.0001$; ***, $p < 0.001$; **, $p < 0.01$; *, $p < 0.05$; ns, $p > 0.05$.

Stacks of confocal images of synaptic boutons stained for Dlg and GluRIIC were analyzed with Imaris to examine the overlap between Dlg and IIC. The ‘Coloc’ function was used to evaluate the colocalization between Dlg and GluRIIC signals and to calculate the Pearson correlation coefficient in the voxel volume.

For the quantification of individual Brp puncta, singles NMJs (muscle 6/7, segment A3) stained for Brp and HRP were assembled from multiple frames (3–4) imaged at a 4.0x zoom. Individual frames were analyzed using ImageJ software for Fiji distribution and maximum intensity projections (Schindelin et al., 2012). The channels were separated and the low intensity Brp-positive removed by applying a threshold and a mask. The ‘RawIntDen’, which represents the total intensity of the Brp signal, and the ‘Area’ of the selection were calculated and added them together to assemble an entire NMJ from different frames. For each genotype, the Brp intensity per unit area (ΣRawIntDen)/(ΣArea) from PhTx treated animals was normalized and reported relative to the untreated larvae. Statistical analyses were performed with Prism7 using the unpaired t test with a two-tailed distribution. For the Brp peak analysis, we measured the intensity of the peaks contained within the selected masks using the Find Maxima algoritm (ImageJ) and normalized them as above. The frequency distribution and cumulative distribution of peak values were calculated with Prism7.

For the quantification of GFP signals in synaptic boutons, z stack imaged NMJs (muscle 6/7, segment A3) stained for Brp, HRP and GFP were converted in maximum intensity projections using Fiji. The channels were separated and a threshold mask was applied to the HRP channel to demarcate the synaptic terminal. The ‘RawIntDen’ of GFP signals within each synaptic terminal was measured. Statistical analyses were performed with Prism using the unpaired t test with a two-tailed distribution.

Super resolution (3D-SIM) imaging and data processing—Super-resolution imaging was performed on a Carl Zeiss Elyra PS1 inverted microscope using a Plan-Apo 100X (1.46 NA) oil immersion objective and an EM-CCD Andor iXon 885 camera. We collected 3 5 phases at 3 3 angles for a total of 15 images per plane. Singles NMJ 6/7 at the A3 segment were captured by multiple frames (3–4 per NMJ); the stacks of z sections were taken at a spacing of every 100 nm. All raw images were processed and reconstructed in 3D using Zen Black 2010 software (Carl Zeiss). The images were also channel aligned using an alignment matrix generated by imaging colored beads. The PSD areas were estimated using the Fiji distribution algorithm (ImageJ) (Schindelin et al., 2012). Single ROIs corresponding to the maximum PSD areas were selected and measured using either the wand tool (with legacy and regulated tolerance) or manually, for overlapping regions. At least 1400 single PSDs from 12 or more different NMJs for each genotype. Statistical analyses were performed with Prism using one-way ANOVA with Tukey’s post hoc test for multiple comparison, frequency distribution and cumulative distribution. Data are presented as mean ± SEM.

Electrophysiology—The standard larval body wall muscle preparation first developed by Jan and Jan (1976) was used for electrophysiological recordings. Wandering third instar larvae were dissected and washed in physiological saline. Using a custom microscope stage

system, all recordings were performed in HL-3 saline (Stewart et al., 1994) containing 0.5 mM $CaCl_2$ unless otherwise indicated. For the acute homeostasis paradigm, semi-intact preparations were incubated with philanthotoxin-343 (PhTx) (Sigma; 20 mM) in Ca^{2+}-free HL-3 saline for 15 min as previously described (Frank et al., 2006). The nerve roots were cut near the exiting site of the ventral nerve cord so that the motor nerve could be picked up by a suction electrode. Intracellular recordings were made from muscle 6, abdominal segment 3 and 4. Data were used when the input resistance of the muscle was > 5 MΩ and the resting membrane potential was < —60 mV. The input resistance of the recording microelectrode (backfilled with 3 M KCl) ranged from 20 to 25 MΩ. Muscle synaptic potentials were recorded using Axon Clamp 2B amplifier (Axon Instruments) and analyzed using pClamp 10 software. Spontaneous miniature excitatory junction potentials (mEJPs) were recorded in the absence of any stimulation. To calculate mEJP mean amplitudes, 50–100 events from each muscle were measured and averaged using the Mini Analysis program (Synaptosoft). Minis with a slow rise and falling time arising from neighboring electrically coupled muscle cells were excluded from analysis. Evoked EJPs were recorded following supra-threshold stimuli (200 μsec) to the appropriate segmental nerve with a suction electrode. Ten to fifteen EJPs evoked by low frequency of stimulation (0.1 Hz) were averaged. QC was calculated by dividing the mean EJP by the mean mEJP after correction of EJP amplitude for nonlinear summation according to previously described methods. Corrected EJP amplitude = E[Ln[E/(E - recorded EJP)]], where E is the difference between reversal potential and resting potential. The reversal potential used in this correction was 0 mV.

For readily-released pool (RRP) measurements, evoked excitatory junction currents (EJCs) were recorded at a voltage clamped to – 65 mV, and 30 EJCs were stimulated at 50 Hz in HL-3 saline with 1.5 mM Ca^{2+} and 10 mM Mg^{2+}. EJC amplitudes during a stimulus train were calculated by subtracting the baseline current just preceding an EJC from the subsequent peak of the EJC. The cumulative EJC amplitude was obtained by back-extrapolating a straight line fitted to the final 10 points of the cumulative EJC to time zero. The size of the RRP were calculated by dividing the cumulative EJC amplitude by the mean mEJP amplitude recorded in the same muscle. Statistical analyses were performed with Prism using ANOVA followed by a Tukey's post hoc test. Data are presented as mean ± SEM.

Presynaptic Ca^{2+} imaging—Cytosolic Ca^{2+} levels were monitored through the fluorescence of a Ca^{2+}-sensitive dye (Oregon-Green BAPTA-1; OGB-1) relative to a Ca^{2+}-insensitive dye (Alexa Fluor 568; AF568); both of which were loaded into motor neuron terminals using the forward-filling technique as previously described (Macleod, 2012). Segment nerves were forward-filled with 10,000 MW dextran-conjugated OGB-1, in constant ratio with 10,000 MW dextran-conjugated AF568. Fluorescence imaging was performed through a water-dipping 100X 1.1 NA Nikon objective fitted to an upright Nikon Eclipse FN1 microscope. Fluorescence was excited using a Lumencor Spectra X light engine (OGB-1: 483/32 nm; AF568: 550/15 nm). Emitted light (OGB-1: 525/84 nm; AF568: 605/52 nm) was captured by an Andor iXon3 897 EMCCD camera running at 112 frames-per-second (2×2 binning, 8 ms exposures). OGB-1 images were not interdigitated with

AF568 images during the stimulus protocol, rather, AF568 fluorescence images were captured immediately before and after the stimulus protocol to provide ratio information. While larvae were dissected and incubated in Schneider's insect medium, this medium was replaced with HL3 at least 20 minutes prior to imaging. HL3 was supplemented with 0.5 mM Ca^{2+}, 20 mM Mg^{2+}, and 7 mM L-glutamic acid, which prevents muscle contraction (Macleod et al., 2004). Segmental nerves were stimulated according to the pattern illustrated in Figure 6A, where each fluorescence transient is the result of an impulse of approximately 1.5 V applied to the nerve for 0.4 ms. The background fluorescence was subtracted from each image and the average pixel intensity was measured within a region-of-interest containing 2–5 non-terminal boutons using NIS-Elements AR software (Nikon). Fluorescence intensity traces were further processed in ImageJ [Fiji (fiji.sc; ImageJ)]. OGB-1 fluorescence was imaged for 5 s prior to the first stimulus pulse, and these data were used to estimate the OGB-1 bleach trend which was then numerically removed from the entire trace. Ca^{2+} levels are expressed as the fluorescence ratio of OGB-1 to AF568. Fluorescence transients corresponding to the action potentials evoked at 1 Hz were numerically averaged into a single trace and used to calculate peak amplitude and the decay time constant (t). The amplitude of a single transient was calculated as the displacement between the baseline prior to the transient and the mono-exponential fit to the transient decay when extrapolated backward to the time of the nerve stimulus. Two criteria were used to exclude data from further analysis; first, when the data were collected from a terminal with a resting Ca^{2+} level that was assessed to be an outlier, and second, when single action potential evoked fluorescence transients did not recover to baseline with a time course of less than 150 ms. Outliers were defined using the median absolute deviation (MAD; (Leys et al., 2013)) where an outlier was considered to be any value beyond 3X MAD of the median. Differences between *neto-α*^{null} and control were tested using the Students T statistic, and where normality tests failed, the Mann Whitney U statistic was used.

Electron microscopy—For transmission electron microscopy (TEM), *Drosophila* larva fillets were fixed in 2% glutaraldehyde/2% formaldehyde/2 mM CaCl2 in 0.1 M cacodylate buffer pH 7.4 for 15 min at room temperature followed by 1 hour on ice in fresh fixative. After 5 washes in the buffer, they were post-fixed in 2% osmium tetroxide in the same buffer for 2 hours on ice, washed once in the buffer and 5 times in double distilled water. The samples were than stained *en bloc* overnight in 2% aqueous uranyl acetate, washed 5x in water, dehydrated in series of ethanol concentrations and penetrated with EMbed 812 (EMS, Hatfield, PA). For easy orientation, the fillets were placed on a glass coverslip with the inside facing glass and embedded in the same resin subsequently polymerized at 65°C. The coverslip was removed using hydrofluoric acid; blocks containing fillets were cut out, re-mounted on holders inside facing out and cut parallel to the original glass surface. Semi-thin (200 nm) sections were cut, stained with toluidine blue and checked under light microscope. Once the exact position of cutting was reached, serial thin (80 nm) sections of the fillets were cut on Leica EM UC7 microtome (Leica, Deerfield, IL) and stained with uranyl acetate. The samples were examined on FEI Tecnai 20 TEM (FEI, Hillsboro OR) operated at 120 kV and images were recorded on AMT XR81 CCD camera (AMT, Woburn, MA). PSDs and T-bars metrics were quantified from 3–5 serial sections by selecting the maximum PSD

length, T-bar platform and pedestal. The numbers of PSDs examined: 10 control and 14 *neto-α*^{null}; and the number of T-bars: 8 control and 12 *neto-α*^{null}.

QUANTIFICATION AND STATISTICAL ANALYSIS

To quantify immunohistochemistry data, confocal or 3D-SIM images were exported as maximum projections or single confocal sections by ZEN (Carl Zeiss). Photoshop (Adobe) was used for image rotation and cropping. ImageJ (NIH) and Imaris (Bitplane) were used for image quantification and signal co-localization. Excel (Microsoft) and Prism (GraphPad) were used for data analysis and plotting. For pairwise comparisons we used t test, while for comparisons involving more than two genotypes/conditions we used one-way ANOVA followed by Tukey's post hoc test. Data are represented as means ± SEM. In all graphs, *p* values are depicted as follows: ****, $p < 0.0001$; ***, $p < 0.001$; **, $p < 0.01$; *, $p < 0.05$; ns, $p > 0.05$. We considered statistically significant all $p < 0.05$.

No statistical methods were used to determine sample sizes, but our sample sizes were similar to those generally employed in the field. For NMJs morphometric analysis, "n" represents the number of individual synaptic boutons (Figure 1I) or individual NMJs examined (Figure 1, all panels except for 1I) and is indicated in each bar. To evaluate the PSD size (Figures 3E–3J), for each genotype we analyzed at least 1,400 individual PSDs from 12 or more different NMJs. To determine BRP peak intensity distributions, we examined more than 14,000 single active zones from at least 19 different NMJs per genotype and per condition as indicated in each bar (Figure 6K). For electrophysiological recordings, "n" represents individual NMJs/animals examined (one NMJ per animal) and is reported in the last column of the Table S1. In general, we used t test to compare average measurements before and after the PhTx treatment in each genotype, and one-way ANOVA to report differences relative to control.

Supplementary Material

Refer to Web version on PubMed Central for supplementary material.

ACKNOWLEDGMENTS

T.H.H., R.V., C.I.R., Q.W., P.N., and M.S. were supported by NIH NICHD awards ZIA HD008914 and ZIA HD008869. G.T.M., R.X.H., and M.S. were supported by NIH NINDS award NS061914. We thank Tom Brody and members of the Serpe laboratory for discussions on this manuscript. We thank Bloomington Stock Center at Indiana University for fly stocks and Developmental Studies Hybridoma Bank at the University of Iowa for antibodies.

REFERENCES

Alberstein R, Grey R, Zimmet A, Simmons DK, and Mayer ML (2015). Glycine activated ion channel subunits encoded by ctenophore glutamate receptor genes. Proc. Natl. Acad. Sci. USA 112, E6048–E6057. [PubMed: 26460032]

Banovic D, Khorramshahi O, Owald D, Wichmann C, Riedt T, Fouquet W, Tian R, Sigrist SJ, and Aberle H. (2010). *Drosophila* neuroligin 1 promotes growth and postsynaptic differentiation at glutamatergic neuromuscular junctions. Neuron 66, 724–738. [PubMed: 20547130]

Budnik V, Koh YH, Guan B, Hartmann B, Hough C, Woods D, and Gorczyca M. (1996). Regulation of synapse structure and function by the Drosophila tumor suppressor gene dlg. Neuron 17, 627–640. [PubMed: 8893021]

Copits BA, and Swanson GT (2012). Dancing partners at the synapse: auxiliary subunits that shape kainate receptor function. Nat. Rev. Neurosci. 13, 675–686. [PubMed: 22948074]

Davis GW, and Müller M. (2015). Homeostatic control of presynaptic neurotransmitter release. Annu. Rev. Physiol. 77, 251–270. [PubMed: 25386989]

Davis GW, DiAntonio A, Petersen SA, and Goodman CS (1998). Postsynaptic PKA controls quantal size and reveals a retrograde signal that regulates presynaptic transmitter release in *Drosophila*. Neuron 20, 305–315. [PubMed: 9491991]

DiAntonio A. (2006). Glutamate receptors at the *Drosophila* neuromuscular junction. Int. Rev. Neurobiol. 75, 165–179. [PubMed: 17137928]

DiAntonio A, Petersen SA, Heckmann M, and Goodman CS (1999). Glutamate receptor expression regulates quantal size and quantal content at the *Drosophila* neuromuscular junction. J. Neurosci. 19, 3023–3032. [PubMed: 10191319]

Dickman DK, and Davis GW (2009). The schizophrenia susceptibility gene dysbindin controls synaptic homeostasis. Science 326, 1127–1130. [PubMed: 19965435]

Dickman DK, Tong A, and Davis GW (2012). Snapin is critical for presynaptic homeostatic plasticity. J. Neurosci. 32, 8716–8724. [PubMed: 22723711]

Featherstone DE, Rushton E, Rohrbough J, Liebl F, Karr J, Sheng Q, Rodesch CK, and Broadie K. (2005). An essential *Drosophila* glutamate receptor subunit that functions in both central neuropil and neuromuscular junction. J. Neurosci. 25, 3199–3208. [PubMed: 15788777]

Fouquet W, Owald D, Wichmann C, Mertel S, Depner H, Dyba M, Hallermann S, Kittel RJ, Eimer S, and Sigrist SJ (2009). Maturation of active zone assembly by *Drosophila* Bruchpilot. J. Cell Biol. 186, 129–145. [PubMed: 19596851]

Frank CA (2014). Homeostatic plasticity at the *Drosophila* neuromuscular junction. Neuropharmacology 78, 63–74. [PubMed: 23806804]

Frank CA, Kennedy MJ, Goold CP, Marek KW, and Davis GW (2006). Mechanisms underlying the rapid induction and sustained expression of synaptic homeostasis. Neuron 52, 663–677. [PubMed: 17114050]

Frank CA, Pielage J, and Davis GW (2009). A presynaptic homeostatic signaling system composed of the Eph receptor, ephexin, Cdc42, and CaV2.1 calcium channels. Neuron 61, 556–569. [PubMed: 19249276]

Goel P, Li X, and Dickman D. (2017). Disparate Postsynaptic Induction Mechanisms Ultimately Converge to Drive the Retrograde Enhancement of Presynaptic Efficacy. Cell Rep. 21, 2339–2347. [PubMed: 29186673]

Goold CP, and Davis GW (2007). The BMP ligand Gbb gates the expression of synaptic homeostasis independent of synaptic growth control. Neuron 56, 109–123. [PubMed: 17920019]

Gratz SJ, Rubinstein CD, Harrison MM, Wildonger J, and O'Connor-Giles KM (2015). CRISPR-Cas9 Genome Editing in Drosophila. Curr. Protoc. Mol. Biol. 111, 31.2.1–31.2.20. [PubMed: 26131852]

Guan B, Hartmann B, Kho YH, Gorczyca M, and Budnik V. (1996). The *Drosophila* tumor suppressor gene, dlg, is involved in structural plasticity at a glutamatergic synapse. Curr. Biol. 6, 695–706. [PubMed: 8793296]

Han TH, Dharkar P, Mayer ML, and Serpe M. (2015). Functional reconstitution of *Drosophila melanogaster* NMJ glutamate receptors. Proc. Natl. Acad. Sci. USA 112, 6182–6187. [PubMed: 25918369]

He T, Singh V, Rumpal N, and Lnenicka GA (2009). Differences in Ca^{2+} regulation for high-output Is and low-output Ib motor terminals in *Drosophila* larvae. Neuroscience 159, 1283–1291. [PubMed: 19409207]

Jackson AC, and Nicoll RA (2011). The expanding social network of ionotropic glutamate receptors: TARPs and other transmembrane auxiliary subunits. Neuron 70, 178–199. [PubMed: 21521608]

Jan LY, and Jan YN (1976). Properties of the larval neuromuscular junction in *Drosophila melanogaster*. J. Physiol. 262, 189–214. [PubMed: 11339]

Jan LY, and Jan YN (1982). Antibodies to horseradish peroxidase as specific neuronal markers in *Drosophila* and in grasshopper embryos. Proc. Natl. Acad. Sci. USA 79, 2700–2704. [PubMed: 6806816]

Kim YJ, and Serpe M. (2013). Building a synapse: a complex matter. Fly (Austin) 7, 146–152. [PubMed: 23680998]

Kim YJ, Bao H, Bonanno L, Zhang B, and Serpe M. (2012). *Drosophila* Neto is essential for clustering glutamate receptors at the neuromuscular junction. Genes Dev. 26, 974–987. [PubMed: 22499592]

Kim YJ, Igiesuorobo O, Ramos CI, Bao H, Zhang B, and Serpe M. (2015). Prodomain removal enables neto to stabilize glutamate receptors at the *Drosophila* neuromuscular junction. PLoS Genet. 11, e1004988.

Kiragasi B, Wondolowski J, Li Y, and Dickman DK (2017). A Presynaptic Glutamate Receptor Subunit Confers Robustness to Neurotransmission and Homeostatic Potentiation. Cell Rep. 19, 2694–2706. [PubMed: 28658618]

Kittel RJ, Wichmann C, Rasse TM, Fouquet W, Schmidt M, Schmid A, Wagh DA, Pawlu C, Kellner RR, Willig KI, et al. (2006). Bruchpilot promotes active zone assembly, Ca2+ channel clustering, and vesicle release. Science 312, 1051–1054. [PubMed: 16614170]

Lerma J, and Marques JM (2013). Kainate receptors in health and disease. Neuron 80, 292–311. [PubMed: 24139035]

Leys C, Ley C, Klein O, Bernard P, and Licata L. (2013). Detecting outliers: Do not use standard deviation around the mean, use absolute deviation around the median. J. Exp. Soc. Psychol. 49, 764–766.

Li Y, Dharkar P, Han TH, Serpe M, Lee CH, and Mayer ML (2016). Novel Functional Properties of *Drosophila* CNS Glutamate Receptors. Neuron 92, 1036–1048. [PubMed: 27889096]

Li X, Goel P, Chen C, Angajala V, Chen X, and Dickman DK (2018). Synapse-specific and compartmentalized expression of presynaptic homeostatic potentiation. eLife 7, e34338.

Littleton JT, and Ganetzky B. (2000). Ion channels and synaptic organization: analysis of the *Drosophila* genome. Neuron 26, 35–43. [PubMed: 10798390]

Lomash RM, Sheng N, Li Y, Nicoll RA, and Roche KW (2017). Phosphorylation of the kainate receptor (KAR) auxiliary subunit Neto2 at serine 409 regulates synaptic targeting of the KAR subunit GluK1. J. Biol. Chem. 292, 15369–15377. [PubMed: 28717010]

Lu Z, Chouhan AK, Borycz JA, Lu Z, Rossano AJ, Brain KL, Zhou Y, Meinertzhagen IA, and Macleod GT (2016). High-Probability Neurotransmitter Release Sites Represent an Energy-Efficient Design. Curr Biol 26, 2562–2571. [PubMed: 27593375]

Macleod GT (2012). Forward-filling of dextran-conjugated indicators for calcium imaging at the *Drosophila* larval neuromuscular junction. Cold Spring Harb. Protoc. 2012, 791–796. [PubMed: 22753611]

Macleod GT, Marin L, Charlton MP, and Atwood HL (2004). Synaptic vesicles: test for a role in presynaptic calcium regulation. J. Neurosci. 24, 2496–2505. [PubMed: 15014125]

Marrus SB, Portman SL, Allen MJ, Moffat KG, and DiAntonio A. (2004). Differential localization of glutamate receptor subunits at the *Drosophila* neuromuscular junction. J. Neurosci. 24, 1406–1415. [PubMed: 14960613]

Mayer ML (2017). The Challenge of Interpreting Glutamate-Receptor Ion-Channel Structures. Biophys. J. 113, 2143–2151. [PubMed: 28844473]

Milstein AD, and Nicoll RA (2008). Regulation of AMPA receptor gating and pharmacology by TARP auxiliary subunits. Trends Pharmacol. Sci. 29, 333–339. [PubMed: 18514334]

Mosca TJ, Hong W, Dani VS, Favaloro V, and Luo L. (2012). Trans-synaptic Teneurin signalling in neuromuscular synapse organization and target choice. Nature 484, 237–241. [PubMed: 22426000]

Müller M, and Davis GW (2012). Transsynaptic control of presynaptic Ca^{2+} influx achieves homeostatic potentiation of neurotransmitter release. Curr. Biol. 22, 1102–1108. [PubMed: 22633807]

Müller M, Pym EC, Tong A, and Davis GW (2011). Rab3-GAP controls the progression of synaptic homeostasis at a late stage of vesicle release. Neuron 69, 749–762. [PubMed: 21338884]

Müller M, Liu KS, Sigrist SJ, and Davis GW (2012). RIM controls homeostatic plasticity through modulation of the readily-releasable vesicle pool. J. Neurosci. 32, 16574–16585. [PubMed: 23175813]

Ng D, Pitcher GM, Szilard RK, Sertié A, Kanisek M, Clapcote SJ, Lipina T, Kalia LV, Joo D, McKerlie C, et al. (2009). Neto1 is a novel CUB-domain NMDA receptor-interacting protein required for synaptic plasticity and learning. PLoS Biol. 7, e41.

Orr BO, Fetter RD, and Davis GW (2017). Retrograde semaphorin-plexin signalling drives homeostatic synaptic plasticity. Nature 550, 109–113. [PubMed: 28953869]

Perrais D, Veran J, and Mulle C. (2010). Gating and permeation of kainate receptors: differences unveiled. Trends Pharmacol. Sci. 31, 516–522. [PubMed: 20850188]

Petersen SA, Fetter RD, Noordermeer JN, Goodman CS, and DiAntonio A. (1997). Genetic analysis of glutamate receptors in *Drosophila* reveals a retrograde signal regulating presynaptic transmitter release. Neuron 19, 1237–1248. [PubMed: 9427247]

Petzoldt AG, Lee YH, Khorramshahi O, Reynolds E, Plested AJ, Herzel H, and Sigrist SJ (2014). Gating characteristics control glutamate receptor distribution and trafficking *in vivo*. Curr. Biol. 24, 2059–2065. [PubMed: 25131677]

Pinheiro PS, Perrais D, Coussen F, Barhanin J, Bettler B, Mann JR, Malva JO, Heinemann SF, and Mulle C. (2007). GluR7 is an essential subunit of presynaptic kainate autoreceptors at hippocampal mossy fiber synapses. Proc. Natl. Acad. Sci. USA 104, 12181–12186. [PubMed: 17620617]

Qin G, Schwarz T, Kittel RJ, Schmid A, Rasse TM, Kappei D, Ponimaskin E, Heckmann M, and Sigrist SJ (2005). Four different subunits are essential for expressing the synaptic glutamate receptor at neuromuscular junctions of *Drosophila*. J. Neurosci. 25, 3209–3218. [PubMed: 15788778]

Ramos CI, Igiesuorobo O, Wang Q, and Serpe M. (2015). Neto-mediated intracellular interactions shape postsynaptic composition at the *Drosophila* neuromuscular junction. PLoS Genet. 11, e1005191.

Ren X, Sun J, Housden BE, Hu Y, Roesel C, Lin S, Liu LP, Yang Z, Mao D, Sun L, et al. (2013). Optimized gene editing technology for *Drosophila melanogaster* using germ line-specific Cas9. Proc. Natl. Acad. Sci. USA 110, 19012–19017. [PubMed: 24191015]

Schindelin J, Arganda-Carreras I, Frise E, Kaynig V, Longair M, Pietzsch T, Preibisch S, Rueden C, Saalfeld S, Schmid B, et al. (2012). Fiji: an open-source platform for biological-image analysis. Nat. Methods 9, 676–682. [PubMed: 22743772]

Sheng N, Bemben MA, DÍaz-Alonso J, Tao W, Shi YS, and Nicoll RA (2018). LTP requires postsynaptic PDZ-domain interactions with glutamate receptor/auxiliary protein complexes. Proc. Natl. Acad. Sci. USA 115, 3948–3953. [PubMed: 29581259]

Stewart BA, Atwood HL, Renger JJ, Wang J, and Wu CF (1994). Improved stability of *Drosophila* larval neuromuscular preparations in haemolymph-like physiological solutions. J. Comp. Physiol. A Neuroethol. Sens. Neural Behav. Physiol. 175, 179–191.

Straub C, Hunt DL, Yamasaki M, Kim KS, Watanabe M, Castillo PE, and Tomita S. (2011). Distinct functions of kainate receptors in the brain are determined by the auxiliary subunit Neto1. Nat. Neurosci. 14, 866–873. [PubMed: 21623363]

Sulkowski MJ, Han TH, Ott C, Wang Q, Verheyen EM, Lippincott-Schwartz J, and Serpe M. (2016). A Novel, Noncanonical BMP Pathway Modulates Synapse Maturation at the Drosophila Neuromuscular Junction. PLoS Genet. 12, e1005810.

Sumioka A, Yan D, and Tomita S. (2010). TARP phosphorylation regulates synaptic AMPA receptors through lipid bilayers. Neuron 66, 755–767. [PubMed: 20547132]

Tang M, Ivakine E, Mahadevan V, Salter MW, and McInnes RR (2012). Neto2 interacts with the scaffolding protein GRIP and regulates synaptic abundance of kainate receptors. PLoS ONE 7, e51433.

Tomita S. (2010). Regulation of ionotropic glutamate receptors by their auxiliary subunits. Physiology (Bethesda) 25, 41–49. [PubMed: 20134027]

Tomita S, and Castillo PE (2012). Neto1 and Neto2: auxiliary subunits that determine key properties of native kainate receptors. J. Physiol. 590, 2217–2223. [PubMed: 22431337]

Tomita S, Chen L, Kawasaki Y, Petralia RS, Wenthold RJ, Nicoll RA, and Bredt DS (2003). Functional studies and distribution define a family of transmembrane AMPA receptor regulatory proteins. J. Cell Biol. 161, 805–816. [PubMed: 12771129]

Tomita S, Adesnik H, Sekiguchi M, Zhang W, Wada K, Howe JR, Nicoll RA, and Bredt DS (2005). Stargazin modulates AMPA receptor gating and trafficking by distinct domains. Nature 435, 1052–1058. [PubMed: 15858532]

Twomey EC, Yelshanskaya MV, Grassucci RA, Frank J, and Sobolevsky AI (2016). Elucidation of AMPA receptor-stargazin complexes by cryoelectron microscopy. Science 353, 83–86. [PubMed: 27365450]

Wagh DA, Rasse TM, Asan E, Hofbauer A, Schwenkert I, Dürrbeck H, Buchner S, Dabauvalle MC, Schmidt M, Qin G, et al. (2006). Bruchpilot, a protein with homology to ELKS/CAST, is required for structural integrity and function of synaptic active zones in *Drosophila*. Neuron 49, 833–844. [PubMed: 16543132]

Walker CS, Brockie PJ, Madsen DM, Francis MM, Zheng Y, Koduri S, Mellem JE, Strutz-Seebohm N, and Maricq AV (2006). Reconstitution of invertebrate glutamate receptor function depends on stargazin-like proteins. Proc. Natl. Acad. Sci. USA 103, 10781–10786. [PubMed: 16818877]

Wang R, Mellem JE, Jensen M, Brockie PJ, Walker CS, Hoerndli FJ, Hauth L, Madsen DM, and Maricq AV (2012). The SOL-2/Neto auxiliary protein modulates the function of AMPA-subtype ionotropic glutamate receptors. Neuron 75, 838–850. [PubMed: 22958824]

Wang T, Jones RT, Whippen JM, and Davis GW (2016). α2δ−3 Is Required for Rapid Transsynaptic Homeostatic Signaling. Cell Rep. 16, 2875–2888. [PubMed: 27626659]

Wang Q, Chiu S-L, Koropouli E, Hong I, Mitchell S, Easwaran TP, Hamilton NR, Gustina AS, Zhu Q, Ginty DD, et al. (2017). Neuropilin-2/PlexinA3 Receptors Associate with GluA1 and Mediate Sema3F-Dependent Homeostatic Scaling in Cortical Neurons. Neuron 96, 1084–1098. [PubMed: 29154130]

Weyhersmüller A, Hallermann S, Wagner N, and Eilers J. (2011). Rapid active zone remodeling during synaptic plasticity. J. Neurosci. 31, 6041–6052. [PubMed: 21508229]

Wyeth MS, Pelkey KA, Yuan X, Vargish G, Johnston AD, Hunt S, Fang C, Abebe D, Mahadevan V, Fisahn A, et al. (2017). Neto Auxiliary Subunits Regulate Interneuron Somatodendritic and Presynaptic Kainate Receptors to Control Network Inhibition. Cell Rep. 20, 2156–2168. [PubMed: 28854365]

Xing G, Gan G, Chen D, Sun M, Yi J, Lv H, Han J, and Xie W. (2014). *Drosophila* neuroligin3 regulates neuromuscular junction development and synaptic differentiation. J. Biol. Chem. 289, 31867–31877. [PubMed: 25228693]

Zhang W, St-Gelais F, Grabner CP, Trinidad JC, Sumioka A, Morimoto-Tomita M, Kim KS, Straub C, Burlingame AL, Howe JR, and Tomita S. (2009). A transmembrane accessory subunit that modulates kainate-type glutamate receptors. Neuron 61, 385–396. [PubMed: 19217376]

Highlights

- Neto-α functions in both pre- and postsynaptic compartments at the *Drosophila* NMJ
- Postsynaptic Neto-αlimits the size of the postsynaptic density
- Presynaptic Neto-αin conjunction with KaiRID regulates basal neurotransmission
- Neto-α enables presynaptic homeostasis via its intracellular domain

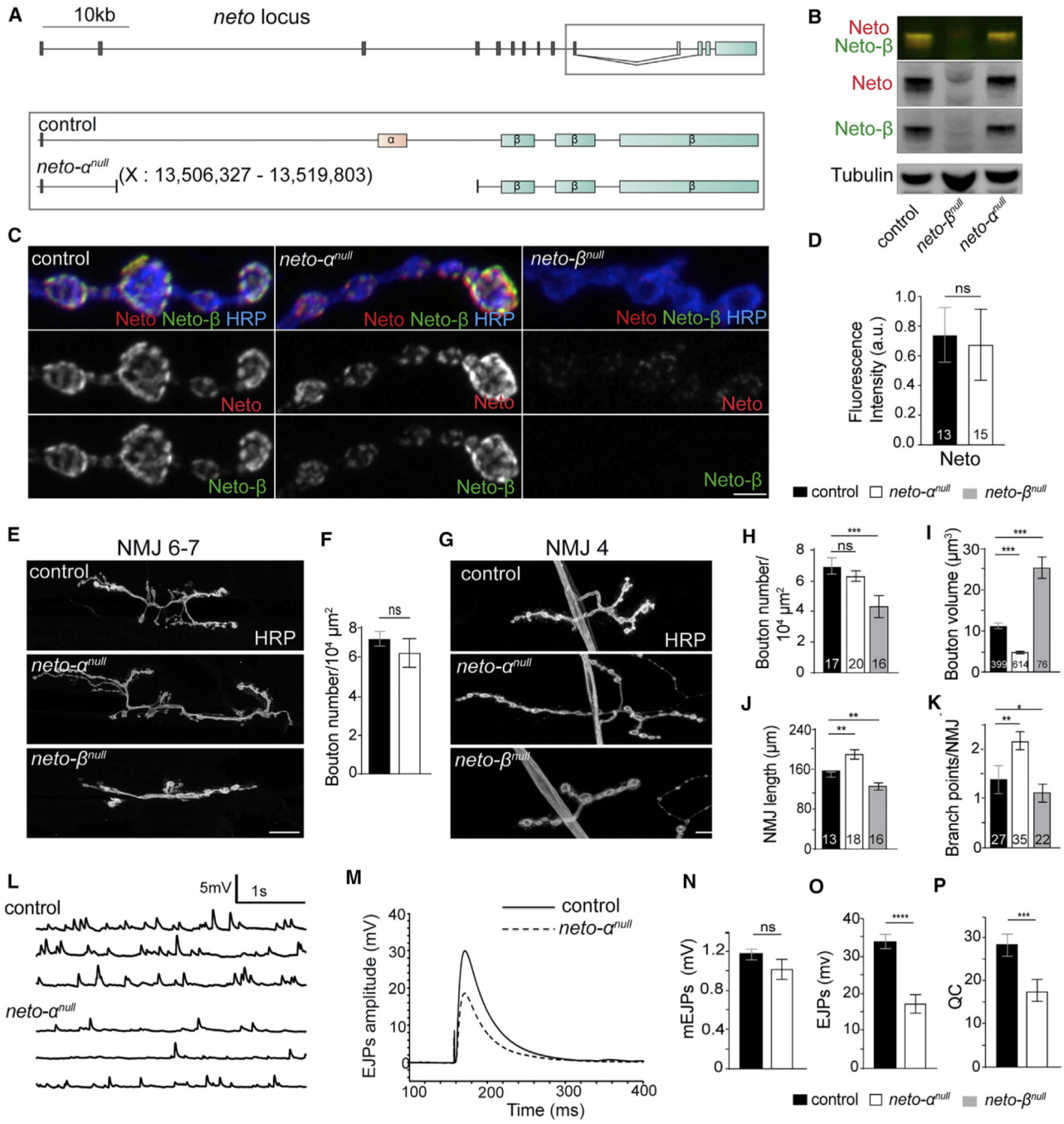

Figure 1. Neto-α Has Different Functions from Neto-β at the NMJ

(A) *Drosophila neto* locus includes 10 shared exons coding for extracellular and transmembrane parts (gray), an exon coding for the Neto-α intracellular domain (pink), and 3 exons coding for the Neto-β intracellular part (blue).

(B) Western blot analysis of muscle extracts from control (w^{1118}), *neto-α*^{null}, and *neto-β*^{null} larvae labeled for Neto (green), Neto-β (red), and Tubulin.

(C) Confocal images of synaptic boutons (NMJ4, segment A3) of the indicated genotypes stained for Neto (red), Neto-β (green), and HRP (blue).

(D) *neto-α*^{null} boutons show normal levels of Neto.

(E–K) Confocal images (E and G) and morphometric quantifications (F and H–K) of NMJ6–7 and NMJ4 (segment A3) in larvae of the indicated genotypes. *neto-α*^{null} NMJs have normal numbers (F and H) but smaller (I) boutons and increased NMJ lengths (J) and branchpoints (K).

(L–P) Representative traces of spontaneous (L) and evoked (M) neurotransmitter release recorded from control (*w*^{1118}) and *neto-α*^{null} third-instar larvae. All data were collected from muscle 6 (A3) in 0.5 mM Ca^{2+} HL-3. Summary bar graphs show the mean amplitude of mEJPs (N), the mean amplitude of EJPs (O), and the QC (P).

Scale bars: 3 mm (C) and 20 mm (E and G). The numbers of NMJs or boutons examined are indicated in each bar. Data are represented as mean ± SEM.****$p < 0.0001$; ***$p < 0.001$; **$p < 0.01$; *$p < 0.05$; not significant (ns), $p > 0.05$.

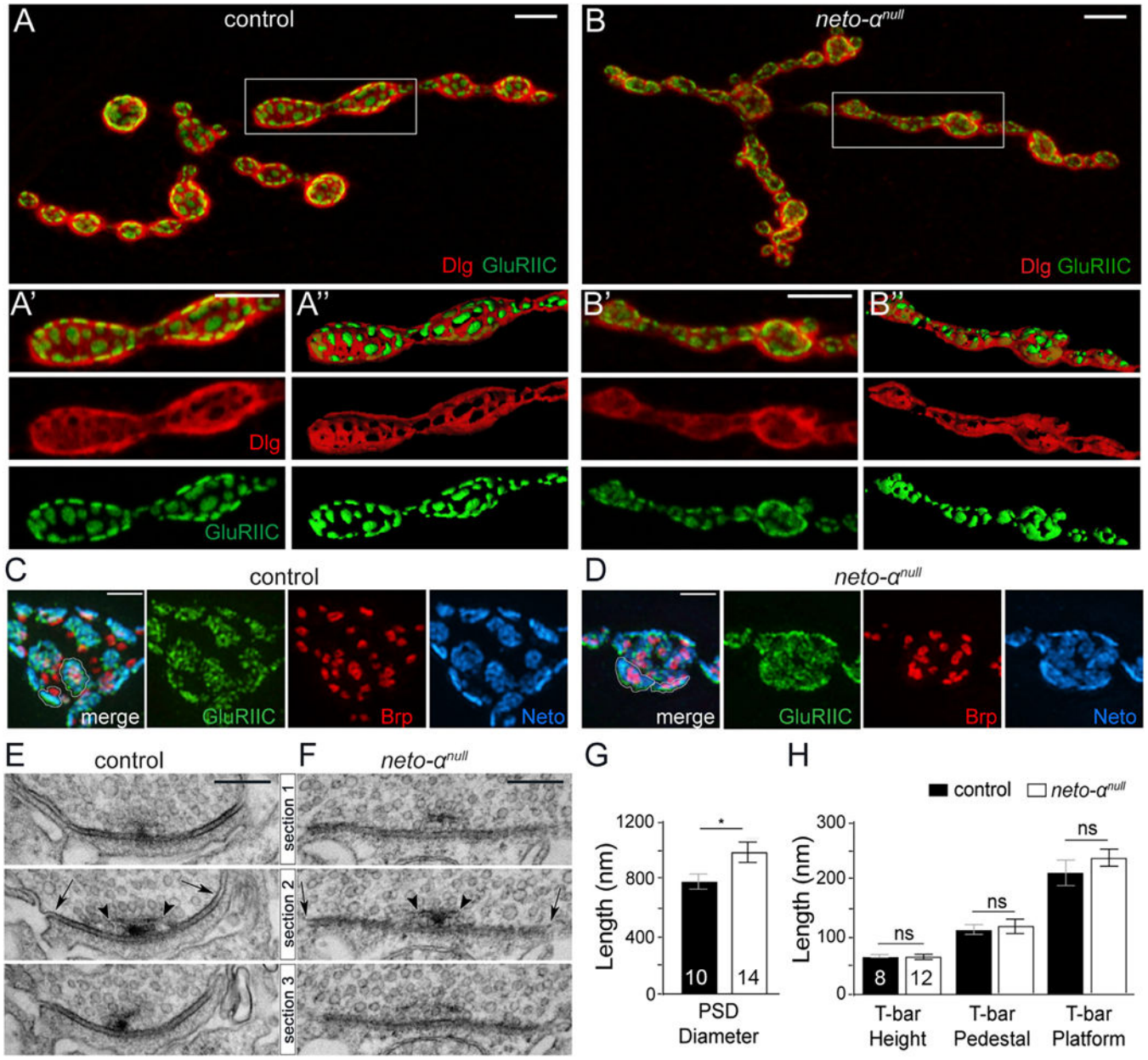

Figure 2. Neto-α Limits the Postsynaptic Receptor Fields

(A–B") Confocal images and 3D reconstitution of NMJ4 boutons labeled with Dlg (red) and GluRIIC (green). In control animals, Dlg-positive staining abuts on GluRIIC-marked PSDs. The borders between Dlg and GluRIIC are blurred in *neto-α^null* boutons (B-B").

(C and D) 3D-SIM images of NMJ4 boutons labeled with Brp (red), GluRIIC (green), and Neto (blue). Individual PSDs are clearly separated in control boutons but are difficult to distinguish in *neto-α^null*.

(E and F) Serial sections of electron micrographs of single PSDs in control (E) and *neto-α^null* boutons (F). The longest diameters detectable in serial sections for each PSD or T-bar structure are indicated by arrows and arrowheads, respectively (E and F) and are quantified (G and H).

Scale bars: 5 μm (A and B), 1 μm (C and D), and 200 nm (E and F). Data are represented as mean ± SEM. *$p < 0.05$; ns, $p > 0.05$.

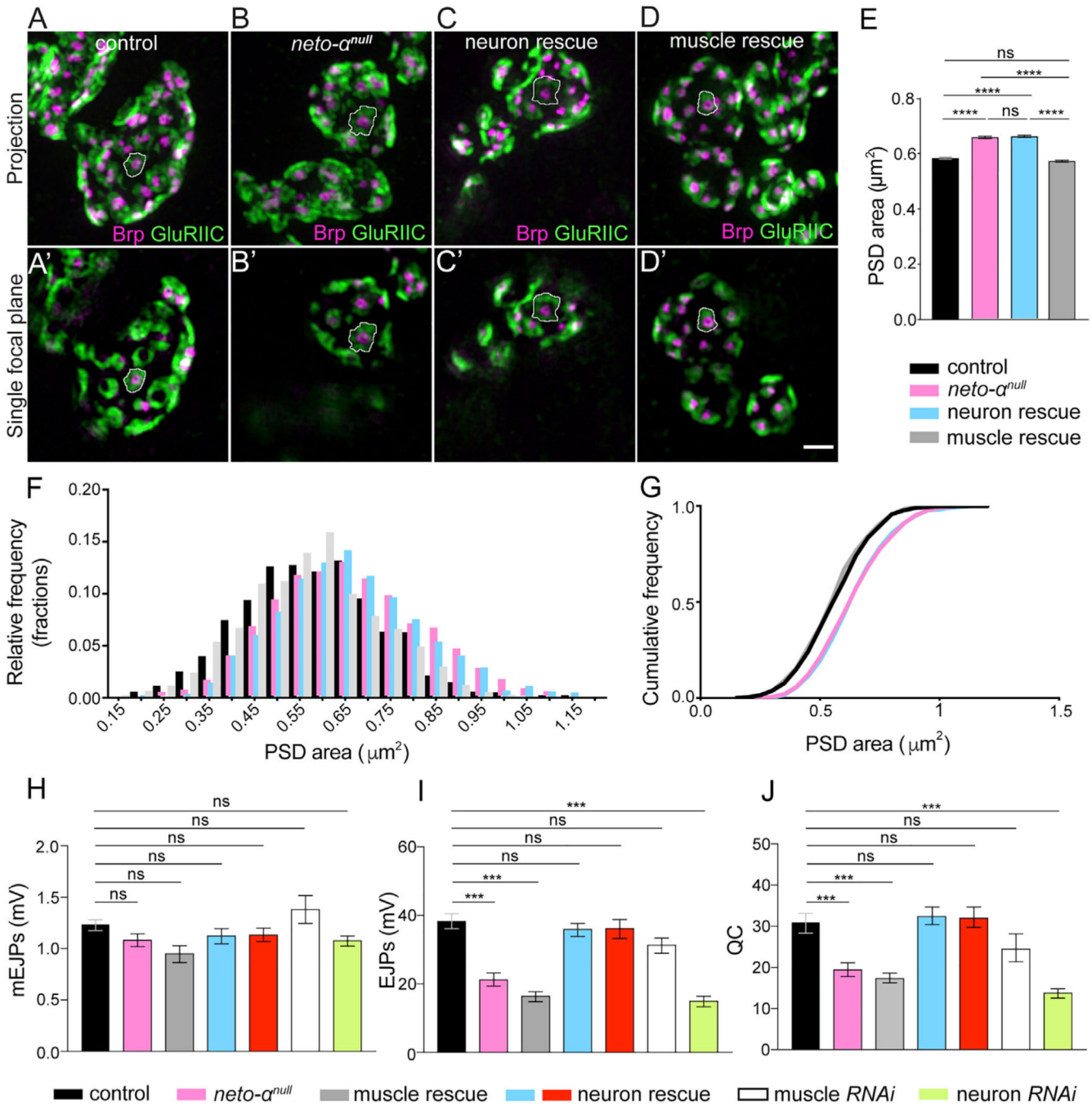

Figure 3. Neto-α Functions in Both Pre- and Postsynaptic Compartments

(A–D) Representative 3D-SIM images (maximum intensity projection and single focal plane) of NMJ4 boutons of the indicated genotypes labeled with Brp (magenta) and GluRIIC (green).

(E) Mean individual PSD areas (white contours) are plotted. Muscle expression, but not neuronal expression, of Neto-α rescues the enlarged PSD size of *neto-α^null^*.

(F and G) Relative and cumulative frequency distribution of different sizes of PSDs. Number of PSDs quantified: control (n = 1,600), *neto-α*^{null} (n = 1,438), neuronal rescue (n = 1,569), muscle rescue (n = 1,600).

(H–J) Summary bar graphs showing the mean amplitude of mEJPs (H), the mean amplitude of EJPs (I), and the QC (J) at NMJ6–7 of the indicated genotypes.

Scale bar: 1 μm. Error bars indicate SEM. ****p < 0.0001; ***p < 0.001; ns, p > 0.05. Genotypes: control (*w*^{1118}), muscle rescue (*neto-α*^{null}*;G14-Gal4/UAS-neto-α*), neuron rescue (*neto-α*^{null}*;OK6-Gal4/UAS-neto-α* and *neto-α*^{null}*,BG380-Gal4/Y;UAS-neto-α/+*), muscle RNAi (*G14-Gal4/+;UAS-neto-α*^{RNAi}*/+*), neuron RNAi (*BG380-Gal4/+;;UAS-neto-α*^{RNAi}*/+*).

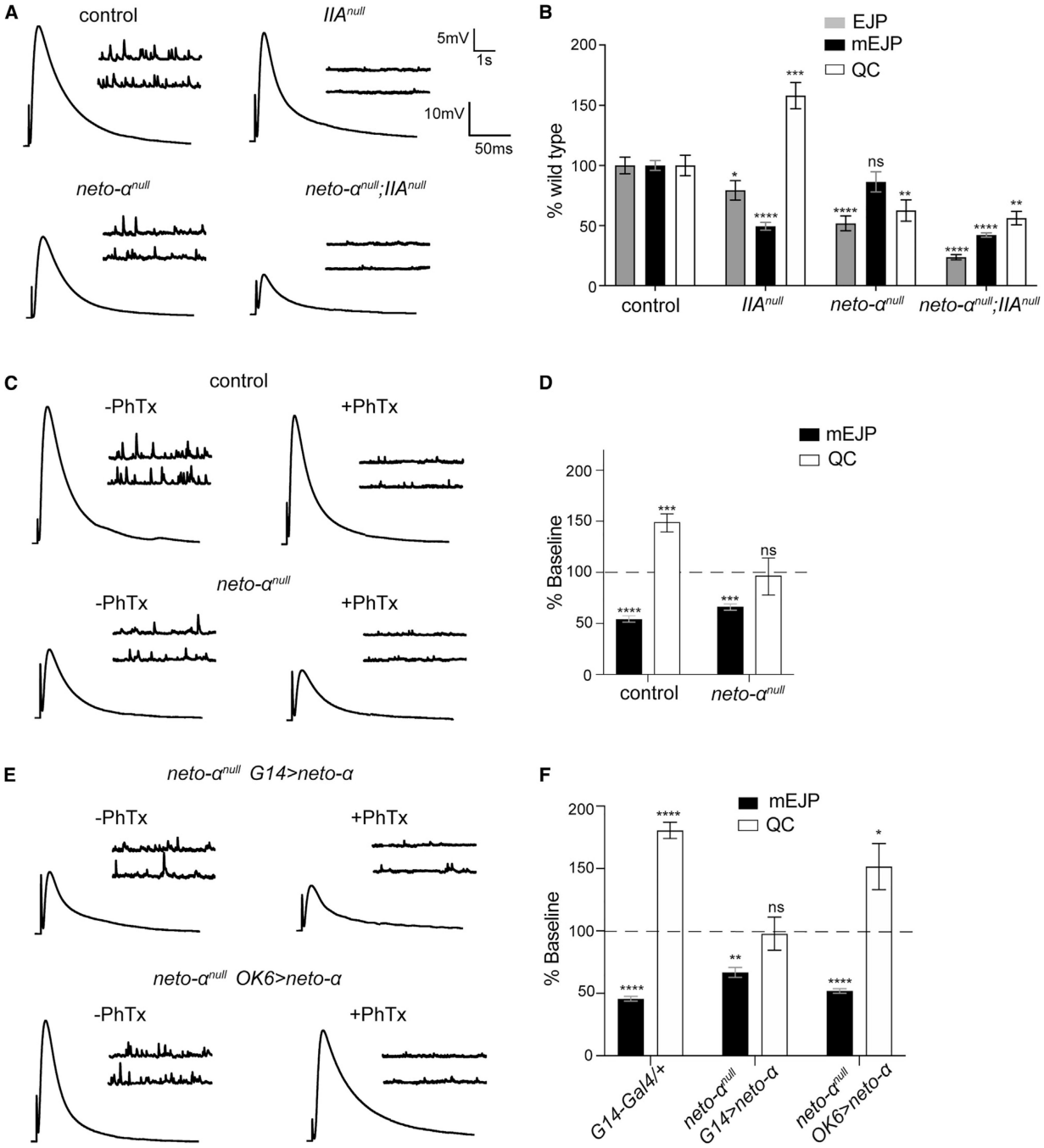

Figure 4. Neto-α Is Required for the Presynaptic Homeostatic Response

(A) Representative traces for mEJP and EJP recordings from muscle 6 of the indicated genotypes.

(B) Quantification of mEJP amplitude and QC values normalized to control (w^{1118}).

(C) Representative traces for mEJP and EJP recordings before and after PhTx treatment in control and *neto-α*^{null} mutants.

(D) Quantification of mEJP amplitude and QC values after PhTx, normalized to the baseline values of the same genotype. Following PhTx application, *neto-α*^{null} mutants fail to restore their basal neurotransmission and show no increase in QC.

(E) Representative traces for mEJP and EJP recordings before and after PhTx application in *neto-α*^{null} mutants rescued by muscle- or neuron-expressed *neto-α*.

(F) Quantification of mEJP amplitude and QC relative values shows QC increase only in neuronally rescued mutants.

Data are represented as mean ± SEM.****$p < 0.0001$; ***$p < 0.001$; **$p < 0.01$; *$p < 0.05$; ns, $p > 0.05$.

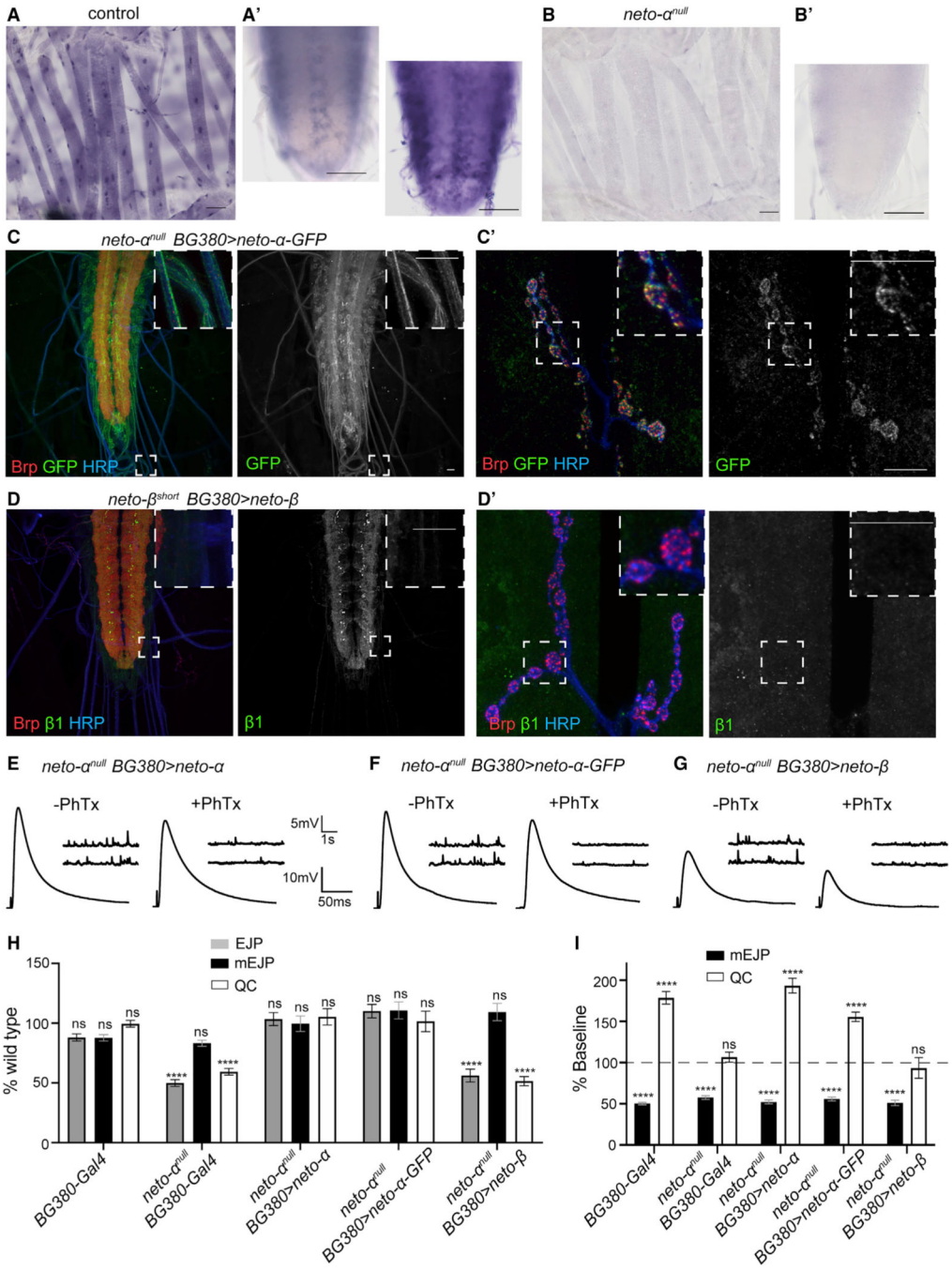

Figure 5. Different Distributions and Functions for Neto-α and Neto-β

(A and B) Expression of *neto-α*-specific exon in the striated muscles and ventral ganglia of third-instar larvae by *in situ* hybridization. Exposures for 10 and 40 min capture a subset of *neto-α*-positive cells in the ventral ganglia (A'). Such cells remained unstained even after a long exposure in *neto-α^null* (B').

(C–D') Confocal images of the ventral ganglia (C and D) and NMJ boutons (C' and D') labeled for Brp (red), GFP or Neto-β1 (green), and HRP (blue), showing the distribution of neuronally expressed Neto-α-GFP (C) and Neto-β (D). Neto-α-GFP labels the MN soma

and axons and accumulates in a punctate pattern at synaptic terminals. Neto-β does not label the axons and could not be detected at synaptic terminals. The anti-b1 antibodies recognize a C-terminal peptide that is missing from *neto-β*^{short}, ensuring unambiguous detection of full-length Neto-β.

(E–G) Representative traces for mEJP and EJP recordings for the indicated genotypes before and after PhTx treatment.

(H) Quantification of mEJP amplitude, EJP amplitude, and QC values normalized to control (*w*^{1118}).

(I) Quantification of mEJP amplitude and QC relative values (after/before PhTx treatment, within the same genotype). Unlike *neto-α* and *neto-α-GFP*, *neto-β* overexpression in MNs cannot rescue the electrophysiological and homeostasis deficits of *neto-α*^{null} mutants.

Scale bars: 50 μm (A and B) and 10 μm (C and D). Data are represented as mean ± SEM.****p < 0.0001; ***p < 0.001; **p < 0.01; ns, p > 0.05.

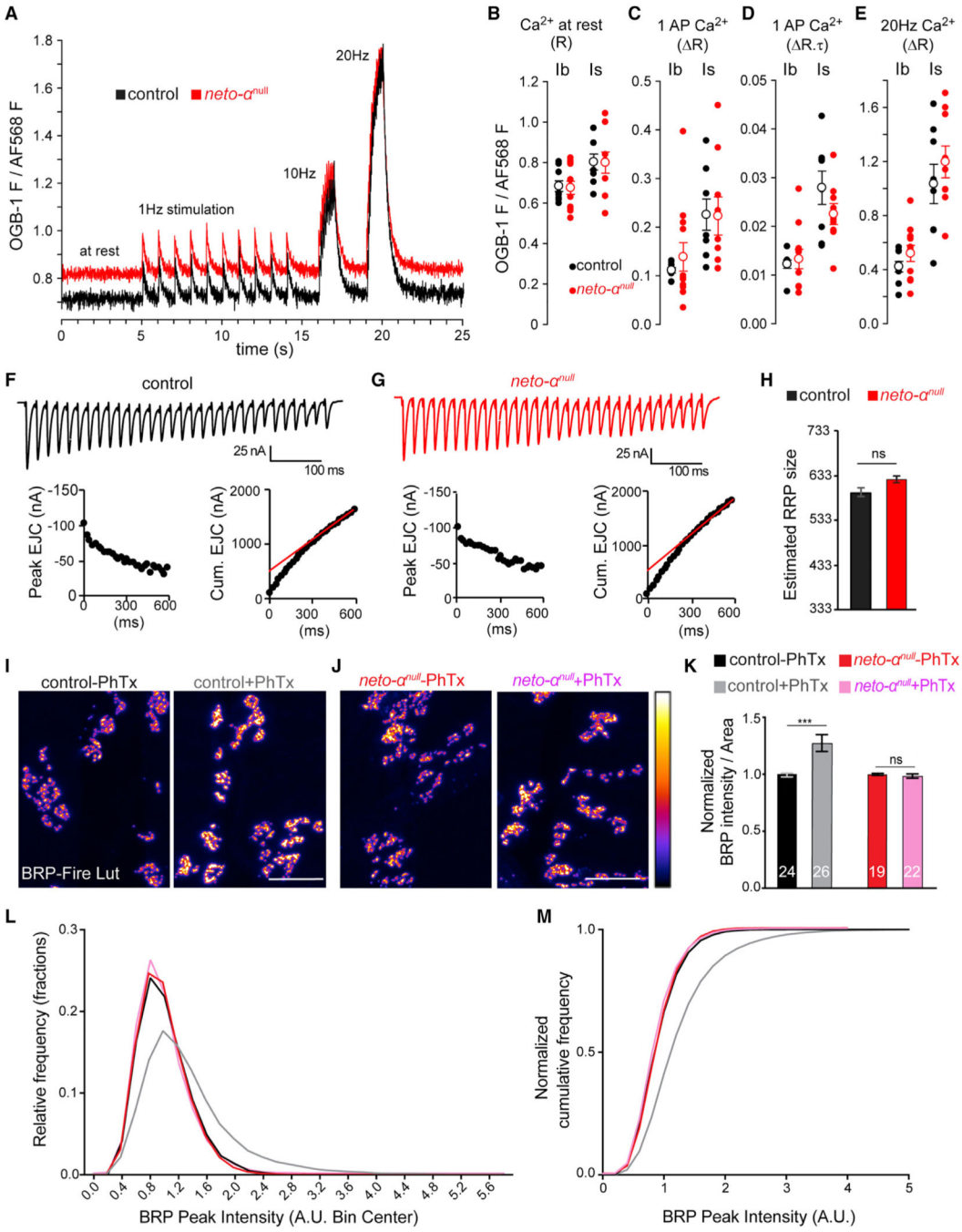

Figure 6. *Neto-α^null* MN Terminals Reveal No Ca^{2+} Entry Deficit, but Cytomatrix Remodeling Is Impaired

(A–E) AP-mediated Ca^{2+} transients are no different in *neto-α^null* MN terminals relative to control. (A) Single-trial traces of changes in Ca^{2+}-sensitive Oregon green BAPTA-1 (OGB-1) fluorescence relative to Ca^{2+}-insensitive Alexa Fluor 568 (AF568) fluorescence in the cytosol of type Ib terminals on muscle 6 in response to stimuli applied to the hemisegment nerve: 10 at 1 Hz, 10 at 10 Hz, and 20 at 20 Hz. OGB-1 images were collected at 112 frames per second. (B) Scatterplot of OGB-1/AF568 fluorescence before nerve stimulation, representing $[Ca^{2+}]_c$ at rest. Each closed circle represents a ratio (R)

measurement from a specific terminal type (Ib or Is) in a different larva. Open circles represent mean ± SEM. (C) Scatterplot of the amplitude (change in ratio [ΔR]) of Ca^{2+} transients evoked by stimuli delivered at 1 Hz. (D) Scatterplot of the product of amplitude (ΔR) and decay time course (t; reported in seconds) of Ca^{2+} transients evoked by 1 Hz stimuli (ΔR.t).

(E) Scatterplot of the amplitude (DR) of Ca^{2+} transients evoked by a 10 Hz train of stimuli. All data were collected from muscle 6, segment A4, in 0.5 mM Ca^{2+} HL-3. The p values from Student's t tests are reported in the text. The Mann-Whitney U test was applied when normality tests failed.

(F and G) Representative EJC traces (top) and cumulative peak EJC amplitudes (bottom) for 30 stimuli at 50 Hz at 1.5 mM Ca^{2+} in control (F) and *neto-α*^{null} (G).

(H) Estimated RRP sizes for control and *neto-α*^{nul} are similar (n = 5, p = 0.1441).

(I–K) Quantification of BRP intensity following 10 min of vehicle or PhTx treatment at control and *neto-α*^{null} NMJs. BRP is showed in Fire-lut; on the intensity scale, white represents peak intensity (20,000 arbitrary units [a.u.]). PhTx application triggers increased Brp signal intensity in control but not in *neto-α*^{null} boutons.

(L and M) Normalized frequency distribution (L) and cumulative frequency (M) of BRP peak intensities reveal a rightward shift after PhTx application for the control animals (from 1 to 1.34, n = 18,312 peaks without and 18,756 with PhTx, $p < 0.0001$), but not for *neto-α*^{null} (from 1 to 0.97, n = 14,063 without and 17,940 with PhTx, $p < 0.0001$).

Scale bars: 10 μm. Data are represented as mean ± SEM. ***$p < 0.001$; ns, $p > 0.05$.

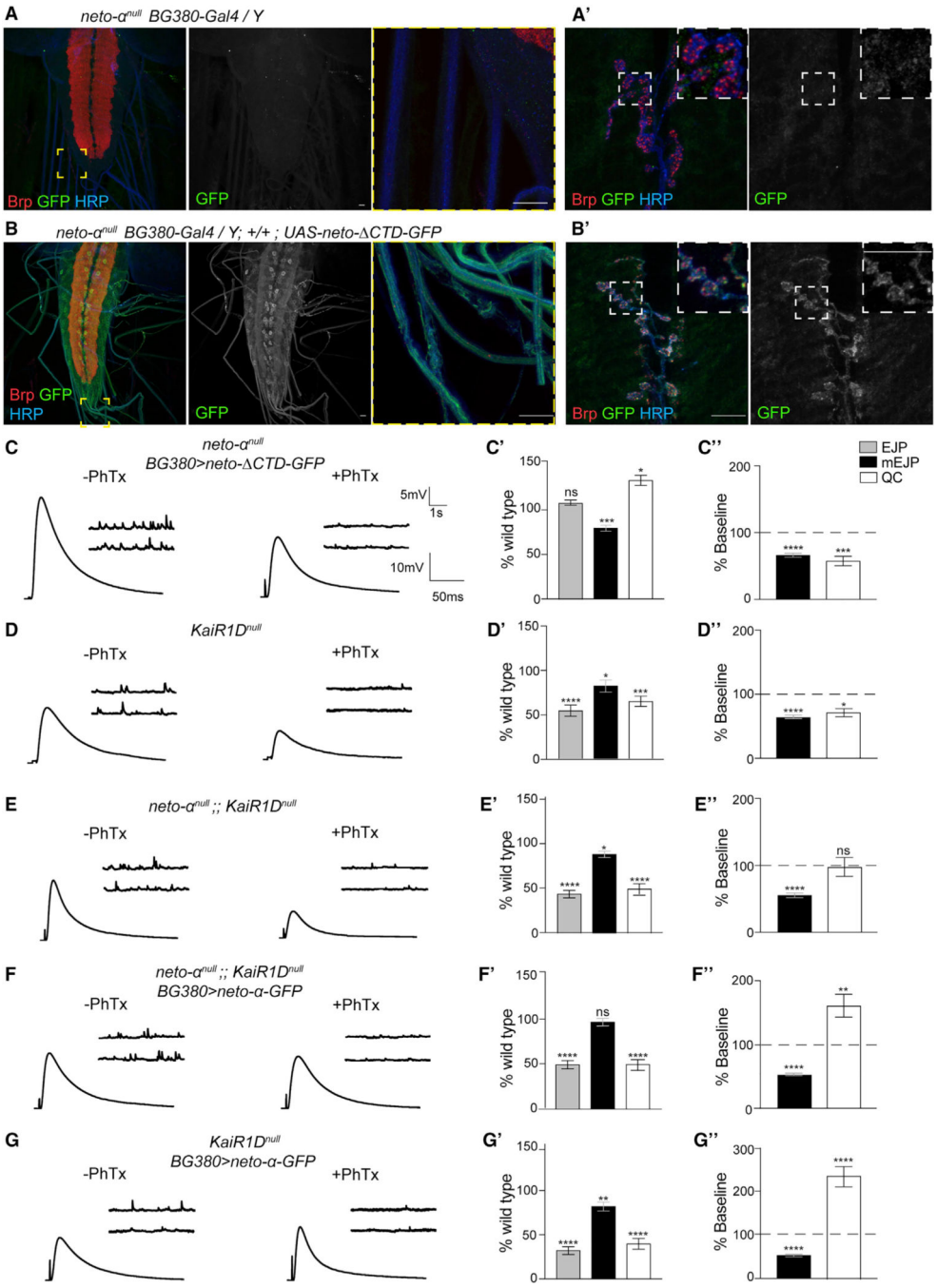

Figure 7. Distinct Domains of Neto-α Regulate Basal Release and Presynaptic Potentiation

(A–B') Confocal images of the ventral ganglia (A and B) and NMJ boutons (A' and B') labeled for Brp (red), GFP (green), and HRP (blue) showing the distribution of Neto-ΔCTD-GFP when overexpressed in MNs (A) and the negative control (B). Similar to Neto-α-GFP (Figure 5C), Neto-ΔCTD-GFP labels the soma and axons of MNs and accumulates at synaptic terminals.

(C–G') Sets of electrophysiological recordings of basal neurotransmission and presynaptic homeostatic potentiation response for the indicated genotypes. Each analysis includes

representative traces for mEJP and EJP recordings before and after PhTx application (left); quantification of mEJP amplitude, EJP amplitude, and QC values normalized to control (w^{1118}) (middle); and quantification of mEJP amplitude and QC relative values after PhTx treatment normalized to the baseline values of the same genotype (right). Neuronal Neto-ΔCTD-GFP rescues basal neurotransmission but cannot restore the homeostatic response at *neto*-a^{null} NMJs (C). The electrophysiological defects of *KaiRID*^{null} NMJs resemble those of *neto-α*^{null} mutants, as well as of *neto-α*^{null}*;;KaiRID*^{null}, suggesting that KaiRID and Neto-α function in the same pathway (D and E) (Figure S5). Overexpression of *neto-α-GFP* in *neto-α*^{null}*;;KaiRID*^{null} MNs does not restore the EJP amplitude but does enable a significant PHP response (F). When *neto-α-GFP* is overexpressed in the presence of endogenous Neto-α, the amplitude of the PHP response is dramatically increased (G).

Scale bars: 10 μm. Data are represented as mean ± SEM. ****p < 0.0001; ***p < 0.001; **p < 0.01; *p < 0.05; ns, p > 0.05.

KEY RESOURCES TABLE

REAGENT/RESOURCE	SOURCE	IDENTIFIER
Antibodies		
mouse anti-GluRIIA	DSHB	MH12B; RRID:AB_528269
mouse anti-Dlg	DSHB	4F3; RRID:AB_528203
mouse anti-Brp	DSHB	Nc82; RRID:AB_2314866
chicken anti-GFP	Abcam	Cat#: ab13970; RRID:AB_300798
mouse anti-α-Tubulin	Sigma-Aldrich	DM1A; RRID:AB_2617116
rat anti-Neto-ex	Custom antibody	N/A
rabbit anti-Neto-β1	Custom antibody	N/A
rabbit anti-GluRIIB	Custom antibody	N/A
rabbit anti-GluRIIC	Custom antibody	N/A
Alexa Fluor 647 goat anti-HRP	Jackson ImmunoResearch Laboratories, Inc	Cat#: 123–605-021; RRID:AB_2338967
Chemicals, Peptides and Recombinant Proteins		
Philanthotoxin-343	Sigma-Aldrich	Cat#: P206
Oregon-Green 488 BAPTA-1 dextran	ThermoFisher	Cat#: O6798
Dextran, Alexa Fluor 568	ThermoFisher	Cat#: D22912
SlowFade Gold with DAPI	Invitrogen	Cat#: S36938
ProLong Gold	Invitrogen	Cat#: P36930
Oligonucleotides		
gRNA α−1 sense	5′P-CTTCGGTTTCTGGGGATAAGATGG	N/A
gRNA α−1 antisense	5′P- AAACCCATCTTATCCCCAGAAACC	N/A
gRNA α−3 sense	5′P- CTTCGGAATATAATGGAAAAATGA	N/A
gRNA α−3 antisense	5′P- AAACTCATTTTTCCATTATATTCC	N/A
Neto-F1	5′-AGTCCCTTTACCACTCCATTAGCC	N/A
Neto-R1	5′-TTGCGAGTGCTTTTGCCTGC	N/A
CG3822-gATD1 sense	5′P- CTTCGCATTTTGAATTCGTTCGCGA	N/A
CG3822-gATD1 antisense	5′P- AAACTCGCGAACGAATTCAAAATGC	N/A
CG3822-gATD2 sense	5′P- CTTCGACAGCTTCCATGCCGGGAAA	N/A
CG3822-gATD2 antisense	5′P- AAACTTTCCCGGCATGGAAGCTGTC	N/A
CG3822-F1	5′-CAAACCCTTGGAGAAATAGGG	N/A
CG3822-R1	5′-CTACGATTGAGGTCCCCTTG	N/A
Software and Algorithms		
Imaris 8.0	Bitplane	N/A
ImageJ 2.0	National Institutes of Health	N/A
Prism 8	GraphPad Software, Inc.	N/A